A measurement of the $W^{\pm}Z$ production cross section and limits on anomalous trilinear gauge couplings in proton-proton collisions at $\sqrt{s} = 7$ TeV using 4.64 fb^{-1} of data collected with the ATLAS detector

DISSERTATION

Presented in Partial Fulfillment of the Requirements for the Degree Doctor of Philosophy in the Graduate School of The Ohio State University

By

Advait Neel Nagarkar, B.S., M.S.

Graduate Program in Physics

The Ohio State University

2012

Dissertation Committee:

Kock Kiam Gan, Advisor

Brian Winer

Junko Shigemitsu

Jay Gupta

Abstract

I present a measurement of the $W^{\pm}Z$ production cross section in the leptonic final states in pp collision at $\sqrt{s} = 7$ TeV and limits on anomalous trilinear gauge couplings, using 4.64 fb^{-1} of data collected using the ATLAS experiment at the LHC. The production cross section has been determined to be $19.0^{+1.4}_{-1.3}$(stat.)$\pm$0.9(syst.)$\pm$0.4(lumi.), in agreement with the Standard Model (SM) expectation of $17.6^{+1.1}_{-1.0}$ pb. A search for anomalous tri-linear gauge couplings has been conducted and limits have been set at the 95% confidence level; the result is consistent with the SM couplings.

Acknowledgments

I want to thank my parents for supporting me in this endeavor.

Vita

May, 2007 ..... B.S., University of Maryland, College Park, MD

September, 2009 ..... M.S., The Ohio State University, Columbus, OH

September, 2007 ..... Graduate Teaching Associate, The Ohio State University, Columbus, OH

September, 2009 ..... Graduate Research Associate, The Ohio State University, Columbus, OH

Fields of Study

Major Field: Physics

Studies in Experimental High Energy Particle Physics - ATLAS experiment: Professor K. K. Gan

Table of Contents

List of Figures

Figure **Page**

List of Tables

List of Abbreviations

aTGC anomalous trilinear gauge coupling. 1, 3, 28, 64, 66, 67, 69

ATLAS A Toroidal LHC ApparatuS. 5, 6, 9, 11, 12, 14, 16, 20, 21, 27, 56, 59, 69

BCM beam conditions monitor. 7

C.I. confidence interval. 67

C.L. confidence level. 67, 69

CERN The European Organization for Nuclear Research. 5, 16, 20

CSC cathode strip chamber. 11, 13

CTP central trigger processor. 16

D3PD thrice derived physics data. 20, 27

DAQ data acquisition. 16

DQ data quality. 30, 38

EB event builder. 16

EF event filter. 16–19, 39

EM electromagnetic. 9–11, 17, 18, 21, 22, 24, 25, 31–33, 36, 44, 46

ESD event summary data. 20

EW electroweak. 2

FCal forward calorimeter. 9, 10

FSR final state radiation. 27, 28, 59

HEC hadronic endcap calorimeter. 9, 10

HV high voltage. 7–10, 12, 13

ID inner detector. 5, 6, 15, 17, 19–21, 24, 25, 31–37, 44, 55

IP interaction point. 5, 6, 10, 16, 21, 23, 24

IR interaction region. 5, 6

ISR initial state radiation. 27

L1 level one. 16–19

L2 level two. 16–19

LAr liquid Argon. 9–11

LHC Large Hadron Collider. 5, 17, 19, 52, 67

MC Monte Carlo. 26–28, 31, 43, 44, 46, 48, 52, 56, 61, 64

MDT monitored drift tube. 11, 12, 14, 23

ME matrix element. 26, 49, 66

MS muon spectrometer. 5, 11, 12, 15, 19, 20, 22–24, 35

NLO next-to leading order. 26, 28

OSSF opposite-sign same flavor. 38

PDF parton distribution function. 26, 28, 49, 50

PMT photomultiplier tube. 11

PS parton shower. 26, 27, 59

PV primary vertex. 21, 31, 33, 34, 36, 37

QCD quantum chromodynamics. 1, 27, 28, 50

QED quantum electrodynamic. 27, 28, 59

QFT quantum field theory. 1

RDO raw data output. 17, 27

ROD read out driver. 16

RoI region of interest. 16, 18, 19

RoIB region of interest builder. 16

ROS read out system. 16

RPC resistive plate chamber. 11, 13, 19

SCT semi-conductor tracker. 6, 7, 20, 21, 32, 36

SF scale-factor. 48, 52–54, 56, 60, 65

SM Standard Model. 1–4, 28, 43, 49, 59, 62, 64, 66, 67, 69

SPS Super Proton Synchrotron. 5

T&P Tag & Probe. 34, 36, 52, 53, 55

TDAQ trigger & data acquisition. 16

TGC thin gap chamber. 11, 13, 19, 66

TR transition radiation. 9

TRT transition radiation tracker. 6, 8, 21, 33, 35, 36

UE underlying event. 26, 27

VEV vacuum expectation value. 2

Chapter 1
Introduction and Theory

The Standard Model (SM) of particle physics has been successful in explaining all non-gravitational interactions of fundamental particles observed to date. The SM predicts that in proton-proton collisions, W- and Z-bosons should be produced in pairs at a low, but measurable, rate. To test this prediction, collision data at a 7 TeV center-of-mass energy from the 2011 run of the LHC collected using the ATLAS detector is analyzed and the cross section for the production of W-bosons in association with Z-bosons is measured. There are production mechanisms allowed by unitarity and renomalizability, beyond those predicted by the SM. Limits are set on the anomalous trilinear gauge couplings (aTGCs) associated with these production mechanisms.

1.1 Standard Model

The SM is a quantum field theory (QFT) constructed as a Yang-Mills gauge theory based on the symmetry group $SU(3) \otimes SU(2) \otimes U(1)$ [1]. The symmetry group describes three of the four fundamental interactions between elementary fermions (i.e. all except gravity) as being mediated by gauge bosons. The internal symmetry of the gauge groups are preserved by interactions between the gauge bosons. The elementary fermions are described as chiral spinors whose left-handed components form doublets and whose right-handed components form singlets under the $SU(2)$ symmetry. The model includes twelve fundamental fermion fields, six quarks (up, down, charm, strange, top, and bottom) and six leptons (electron, muon, τ, and their respective neutrinos) [2].

The quantum chromodynamics (QCD) sector of the SM is defined by the $SU(3)$ sub-group of the SM gauge group. The conserved current associated with the symmetry is called color charge. The generators of the color symmetry, in the fundamental representation of the group, are eight vector boson fields called gluons (g_μ^a). The force described as being mediated by gluons is called the strong nuclear force. The only fermions with non-trivial color charge are the quarks, which can form bound states though strong interactions with

each other.

The electroweak (EW) sector of the SM is defined by the $SU(2) \otimes U(1)$ subgroup of the SM gauge group. The conserved current associated with the $SU(2)$ symmetry is called weak isospin, and that associated with the $U(1)$ symmetry is called weak hypercharge. The generators of the isospin symmetry, in the fundamental representation of the group, are three vector bosons fields called W_μ^a. The generator of the hypercharge symmetry, in the fundamental representation of the group, is a vector boson field called B_μ. There is also a Higgs boson, which is a complex scalar field that couples to all of the fundamental fermions and gauge bosons.

1.1.1 Electroweak Symmetry Breaking

In the vacuum state, the EW symmetry is broken by a non-trivial vacuum expectation value (VEV) of the Higgs boson field into an effective $U(1)$ symmetry. The generator of this effective symmetry, in the fundamental representation of the group, is the vector boson field called the photon (A_μ). The conserved current associated with this effective symmetry is called electric charge, and the force mediated by the photon is called the electromagnetic force. The interactions of particles with the Higgs VEV can be represented as mass terms that couple the left- and right-handed fermion fields to each other and appear as self-interactions of the massive boson fields. The photon field is formed from a linear combination of one of the W_μ^a fields and the B_μ field that has a vanishing effective coupling to the Higgs VEV (i.e. it is massless). The remaining degrees of freedom in those two fields form the electrically neutral massive vector boson field called Z_μ, while the other two isospin fields mix into the electrically charged massive vector boson fields ($W_\mu^\pm$).

1.1.2 Protons

The strong interaction allows for bound states of two up quarks and a down quark (referred to as the three valence quarks). One such bound state is called a proton. The binding interactions can be modeled as virtual particles exchanged between the three valence quarks. In collisions of protons at high energies, such as the 7 TeV collisions studied here, the strong interaction is sufficiently perturbative that the scattering of the protons can be described as a hard interaction between a parton (either one of the valence quarks or one of the virtual particles) from each proton, along with soft interactions between all other partons in the protons.

1.2 $W^{\pm}Z$ Associated Production

1.2.1 Standard Model $W^{\pm}Z$ Production

In proton-proton collisions, the hard scattering interaction can sometimes be modeled as a quark, from one proton, and an anti-quark, from the other, interacting as described by the Feynman diagrams shown in Figure 1.1. In such events, the outgoing particles in the hard scattering are a $W^{\pm}$-boson and a Z-boson. These heavy vectors can decay to lighter particles like charged leptons ($\ell^{\pm}$) and neutrinos (ν). This can result in a final state with a pair of charged leptons from the decay $Z \to \ell^{+}\ell^{-}$ and a charged lepton-neutrino pair from the decay $W^{\pm} \to \ell^{\pm}\nu_{\ell}$. This process has been measured at lower energies by the Tevatron experiments [3, 4]. In this thesis, I present a study of the $\ell^{\pm}\nu_{\ell}\ell'^{+}\ell'^{-}$ final state as a test of the SM.

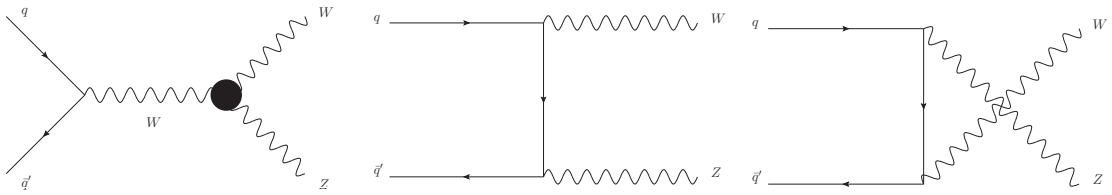

(a) (b) (c)

Figure 1.1: Feynman diagrams describing the SM processes resulting in $W^{\pm}Z$ associated production via the (a) s- (b) t- and (c) u-channels. The s-channel diagram may additionally describe the contributions of processes arising from aTGCs.

1.2.2 Anomalous Trilinear Gauge Couplings

In the Lagrangian of the SM field theory, there are interactions between the vector bosons that preserve the gauge symmetry. When such interactions involve three gauge bosons, they are called trilinear gauge interactions. The s-channel diagram in Figure 1.1a describes the SM $W^{\pm}Z$ production cross section mediated by such interactions. However, the requirements of unitarity, renormalizability, charge conjugation symmetry, and parity conservation allow for three aTGCs (denoted g_1^Z, κ^Z, and λ^Z) in the Lagrangian:

$$\frac{\mathcal{L}_{WWZ}}{g_{WWZ}} = i\left[g_1^Z\left(W_{\mu\nu}^{\dagger}W^{\mu}Z^{\nu} - W_{\mu\nu}W^{\dagger\mu}Z^{\nu}\right) + \kappa^Z W_{\mu}^{\dagger}W_{\nu}Z^{\mu\nu} + \frac{\lambda^Z}{m_W^2}W_{\rho\mu}^{\dagger}W_{\nu}^{\mu}Z^{\nu\rho}\right], \quad (1.1)$$

where $g_{WWZ} = -e\cot\theta_W$ and $X_{\mu\nu} \equiv \partial_\mu X_\nu - \partial_\nu X_\mu$ [5, 6]. Since the SM Lagrangian contains terms of the same form as the g_1^Z and κ^Z terms, those couplings are unity in the SM, and the anomalous couplings are denoted Δg_1^Z and $\Delta\kappa^Z$, where $\Delta\alpha \equiv \alpha - \alpha_{\rm SM}$. These additional interactions form additional mechanisms for $W^\pm Z$ associated production and can therefore be detected as a higher cross section than the SM. These additional production mechanisms lead to enhancement, relative to the SM, at higher $p_{\rm T}$ of the W- and Z-bosons. No such couplings/interactions have been observed to date in searches in $p\bar{p}$ collisions at $\sqrt{s} = 1.96$ TeV [3, 4].

Chapter 2
ATLAS and the LHC

A Toroidal LHC ApparatuS (ATLAS) [7] is a particle detector[1], installed in interaction region (IR) one of the Large Hadron Collider (LHC) [8], hosted by The European Organization for Nuclear Research (CERN) in Geneva, Switzerland. It consists of three main systems, each composed of multiple subsystems: the inner detector (ID) (a charged particle tracking detector), the calorimeter system, and the muon spectrometer (MS); the systems are shown in Figure 2.1. A typical subsystem contains an approximately cylindrical section, called the barrel, in the center and two (one on each side of the barrel) approximately disk shaped sections perpendicular to the z-axis, called endcaps.

2.1 Large Hadron Collider

The ATLAS detector is used to study collisions of bunches of protons, produced and accelerated to an energy of 3.5 TeV by the LHC accelerator chain, as shown in Figure 2.2a.

The LHC is a 27 km circular tunnel located underneath the CERN campus and the surrounding area. It holds two proton beams that are steered in opposite directions though two beam pipes in the tunnel. The beams cross (i.e. switch beam pipes) in eight IRs, numbered one through eight. The point at the center of each IR, where the beams cross each other as they switch beam pipes, are called interaction points (IPs). The two beams are injected from the Super Proton Synchrotron (SPS) into IRs 2 and 8. Bunch trains are injected into the accelerator alternating between beams. When both beams are fully injected with a 50 ns bunch spacing, there are 1380 filled bunches in each ring. Once the injection is complete, the beams are each accelerated to 3.5 TeV, allowing for collisions at 7

[1]The ATLAS detector uses a right-handed cartesian system, relative to an origin at IP1, with the x-axis towards the center of the LHC ring, y-axis in the vertical direction, and z-axis parallel to the beam direction. The longitudinal and transverse directions are defined as being parallel and perpendicular to the z-axis. The regions of the detector with positive and negative z-coordinate are denoted sides A and C respectively. The azimuthal angle (ϕ) is defined relative to the positive x-axis, and the polar angle (θ) is defined relative to the positive z-axis. The pseudorapidity (η) is defined as $\eta \equiv -\ln[\tan(\frac{\theta}{2})]$. The distance in $\eta - \phi$ space (ΔR) is defined as $\Delta R \equiv \sqrt{\Delta\eta^2 + \Delta\phi^2}$.

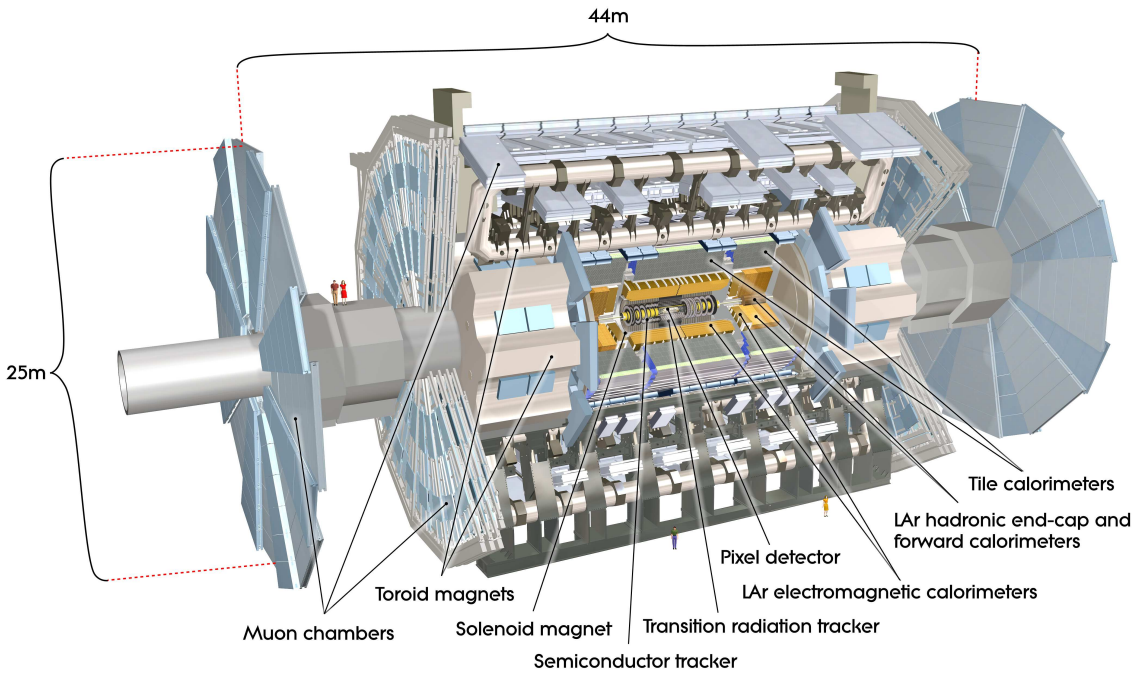

Figure 2.1: The ATLAS detector.

TeV center-of-mass energy. The beams are then squeezed by collimators in IRs 3 and 7 and their positions in the beam pipes are adjusted so that 1331 of the bunches from each beam cross through IP1 in coincidence. During each coincidental bunch crossing, protons from each beam collide (i.e. interact) with protons from the other beam. The beams are held stable in this configuration for as long as possible to allow for the collection of collision data. Once the beams are depleted (i.e. the collision rate decreases by a factor of $\sim$2 due to many protons being scattered away from the beams during collisions), or if there is instability in the beams detected by various beam monitors or experiments along the ring, the beams are dumped into the ground at IR 6. The layout of the LHC ring is shown in Figure 2.2b. The whole process is then repeated with new beams. In 2011, the accelerator was operated around the clock, only pausing for maintenance and development, between April 14th and October 30th. Over this period, the number of bunches per beam was increased gradually to the aforementioned level, and the number of protons per bunch was increased as well, resulting in a much higher rate of collisions at the end of running.

2.2 The ATLAS Inner Detector

The ATLAS ID consists of two precision silicon tracking detectors: the pixel detector and the semi-conductor tracker (SCT), as well as a straw tube tracking detector called the

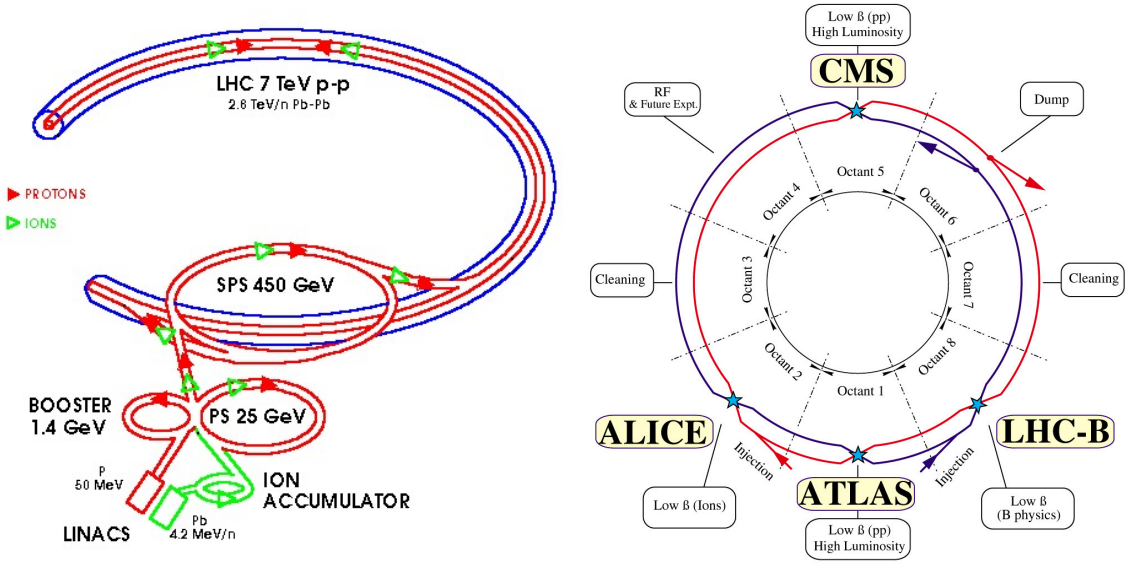

(a) (b)

Figure 2.2: The layout of the LHC (a) accelerator chain and (b) ring.

transition radiation tracker (TRT). The layout of the three trackers is shown in Figure 2.3. The inner detector also includes the beam conditions monitor (BCM) [9], used for luminosity measurement.

2.2.1 Pixel Detector

The pixel detector consists of three layers of modules in the barrel plus three disks of modules in each endcap, covering the region $|\eta| < 2.5$. The innermost layer in the barrel section is called the b-layer. Each module contains a grid of $\sim 300,000$ silicon pixels, each 50×400 μm, located between conducting plates, common on the biased side and pixelated on the readout side, with more than 80 million channels in the whole detector. The pixelated structure allows for the measurement of both the η and ϕ coordinates of charged particles traversing the detector. The modules are biased at HV$\sim$150 V, so that when a charged particle passes through one of the pixels, ionizing electrons in the silicon sensor, a current flows between the plates, registering a physics hit.

2.2.2 Semi-Conductor Tracker

The SCT consists of four layers of silicon strips in the barrel and nine disks of strips in each endcap, also covering the region $|\eta| < 2.5$. Each layer/disk has strips on both sides, where the strips on either side are oriented at relative angle of 40 mrad, with one strip oriented

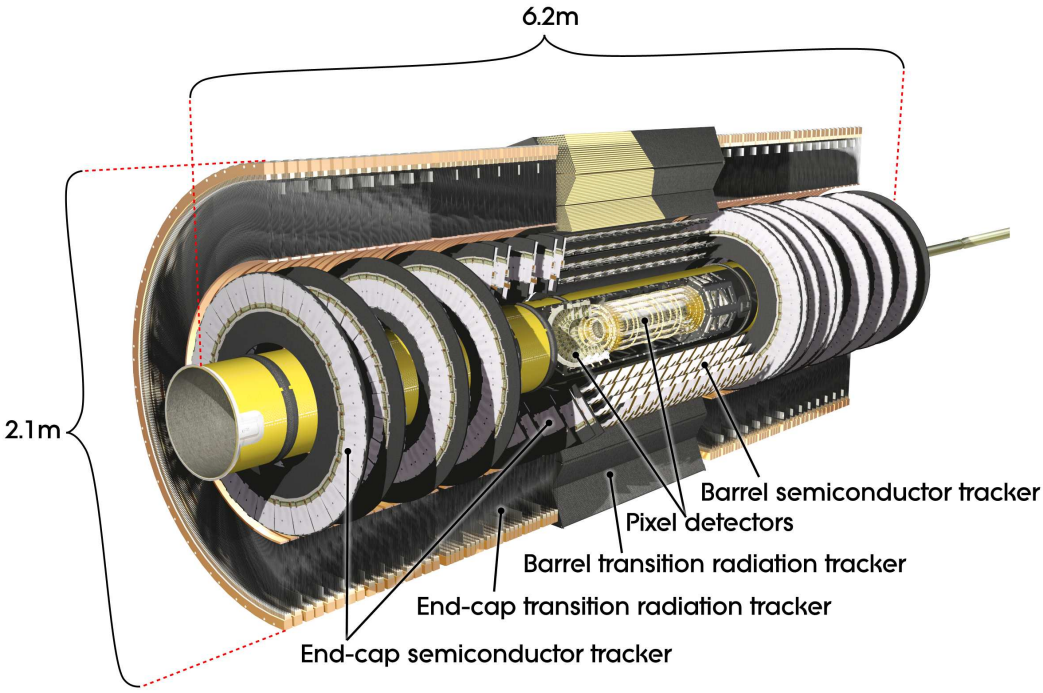

Figure 2.3: The ATLAS inner detector.

longitudinally (radially) in the barrel (endcaps); the stereo angle between strips allows the reconstruction of both the η and ϕ of a charged particle traversing the detector. Each strip is composed of 6.4 cm daisy-chains of silicon sensors with an 80 μm pitch, with more than 6 million channels in the whole detector. The strips are, like the pixels, biased at HV$\sim$150 V, so that when a charged particle traverses the sensor, it produces a current that registers a physics hit.

2.2.3 Transition Radiation Tracker

The TRT consists of 73 planes, each composed of a stack of 144 cm long, 4 mm diameter, aluminum coated polyimide straw tubes, in the barrel and 160 planes, each composed of a stack of 37 cm long tubes, in the endcaps. The TRT covers the region $|\eta| < 2.0$. The straws are all aligned longitudinally (radially) in the barrel (endcaps). This only allows for the measurement of the ϕ coordinate (not the η) of a charged particle traversing the detector. The anode wire along each cathode tube is biased at HV$\sim$ -1500 V. Each tube is filled with a 70%:27%:3% Xe:CO_2:O_2 mixture of gasses. When a charged particle traverses a tube, it ionizes the gas, and the resulting ions further ionize the gas, producing a cascade of additional electrons, as they accelerate towards the anode wire, producing a current through the anode wire that registers a physics hit. Sometimes, relatively energetic particles

will excite some of the nuclei in the gas, which will then emit photons, called transition radiation (TR), as they de-excite. These photons will set off a substantially larger cascade of ionization in the gas. Since different types of particles (e.g. electrons and pions) have different probabilities of producing TR, it is useful to determine which signals are produced by TR. Therefore, the current through the anode wire from each hit is compared to a higher current threshold to determine whether it was a high-threshold physics hit, which information can then be used to identify the type of particle that produced the hit (as discussed in Section 5).

2.2.4 Beam Conditions Monitor

The beam conditions monitor consists of a four-module diamond detector in the forward regions of both sides of ATLAS. The modules are biased at HV, so that when a charged particle passes through one of the modules, ionizing electrons in the diamond substrate, it produces a current that registers a physics hit. The fast signal from the diamond sensors enables the determination of which bunch crossings are coincidences. The count of coincidences provides a measurement of the integrated luminosity of the data sample [10].

2.3 The ATLAS Calorimeters

The ATLAS calorimeter system consists of detectors constructed using two different active materials: liquid Argon (LAr) and scintillating tiles. The layout of the calorimeters is shown in Figure 2.4.

2.3.1 LAr Calorimeters

The calorimeter system has three detectors that use LAr as the active material: the electromagnetic (EM) Calorimeter, the hadronic endcap calorimeter (HEC), and the forward calorimeter (FCal).

Electromagnetic Calorimeter

The EM Calorimeter consists of two sections: a barrel that covers the region $|\eta| < 1.475$ and an endcap that covers the regions $1.375 < |\eta| < 3.2$. The barrel consists of a presampler layer that covers the region $|\eta| < 1.52$, followed by three layers in the region $|\eta| < 1.35$ and two layers in the regions $1.35 < |\eta| < 1.475$. The endcap consists of a presampler layer in the region $1.5 < |\eta| < 1.8$, followed by two layers in the region $|\eta| < 1.5$, three layers in the regions $1.5 < |\eta| < 2.5$, and two layers in the region $2.5 < |\eta| < 3.2$. This allows for at least three layers of coverage within the silicon tracker acceptance. Each layer is composed of cells, each containing layers of sheets of polyimide honeycombs filled with LAr active

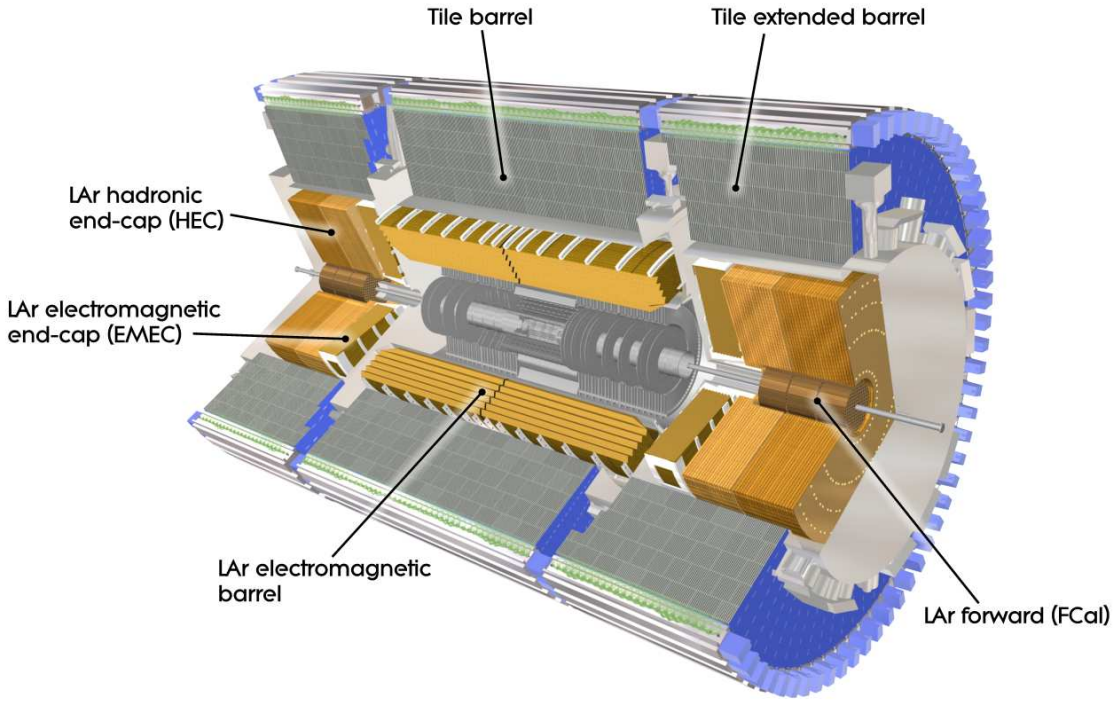

Figure 2.4: The ATLAS calorimeters.

material and sandwiched between electrodes, alternating with layers of accordion shaped lead absorber plates, aligned radially. The anode is biased at HV∼1000-2500 V. When a photon or an electron passes through a calorimeter cell, it interacts with the material, producing a shower of electron-positron pairs and resulting in a current across the electrodes in the cell. The current gives the magnitude of the energy deposition in the cell.

Hadronic Endcap Calorimeter

The HEC consists of two wheels in each endcap. Each wheel contains two segments, composed of cells containing layers of polyimide honeycombs, filled with LAr active material and interleaved with electrodes, placed between layers of flat copper absorber plates, aligned in the transverse plane. It covers the region $1.5 < |\eta| < 3.2$. It functions similarly to the EM calorimeter, with the anodes biased at ~ 1800 V.

Forward Calorimeter

The FCal consists of three modules, along the longitudinal direction, in each endcap. It covers the regions $3.1 < |\eta| < 4.9$. The module in each endcap closest to the IP consists of stacks of copper absorber plates, aligned transversely, with holes drilled in them, aligned

longitudinally. Each hole is filled with a copper cathode tube containing LAr active material and a copper anode rod at the center, held in place by a plastic fiber wrapped around the rod. This module is designed to measure EM showers. The other two modules in each endcap are made of tungsten absorber slugs that surround and space out the copper cathode tubes, and have tungsten anode rods. These modules are designed to measure hadronic showers. The anodes are biased at 250, 375, and 500 V in each successive module.

2.3.2 Tile Calorimeter

The tile calorimeter consists of two sections: a central barrel that covers the region $|\eta| < 1.0$ and an extended barrel on each side that covers the regions $0.8 < |\eta| < 1.7$. Each of the three detectors consists of 64 modules, each of which covers $\Delta\phi = \frac{\pi}{32} \sim 0.1$ and is composed three layers of cells. Each cell contains scintillating polystyrene tiles doped with 2% wavelength-shifting fluors as active material, interleaved with steel absorber plates. The cells in each module are grouped into segments that covers $\Delta\eta = 0.1$. The scintillating tiles in each segment are connected along both sides of the segment via wavelength-shifting fibers that connect to photomultiplier tubes (PMTs) outside of the detector. When a strongly interacting particle passes through a calorimeter cell, it produces a shower of particles that is absorbed by the detector. The absorbed energy is emitted by the scintillating tiles as light, which is passed through the fibers into the PMT. The current produced by the PMT gives the magnitude of the energy deposition in the cell.

2.4 The ATLAS Muon Spectrometer

The ATLAS MS consists of three layers of precision detectors covering the region $|\eta| < 2.7$, constructed using combinations of two types of detector subsystems: monitored drift tubes (MDTs) chambers and cathode strip chambers (CSCs). The three precision layers each are interspaced by and associated with groups, called stations, of layers of detectors, constructed using combinations of two additional types of detector subsystems: resistive plate chambers (RPCs) and thin gap chambers (TGCs). These detectors, called trigger chambers, can be read out with a coarse or fine resolution, for low-level trigger or muon reconstruction (both for higher-level trigger and offline analysis) respectively. The region $2.4 < |\eta| < 2.7$ has fewer layers of trigger chambers, and is therefore not used for the trigger. When the precision layers are used (e.g. in offline analysis), they are considered to be part of the stations with which they are associated. The arrangement of subsystems within the spectrometer are shown in Figure 2.5.

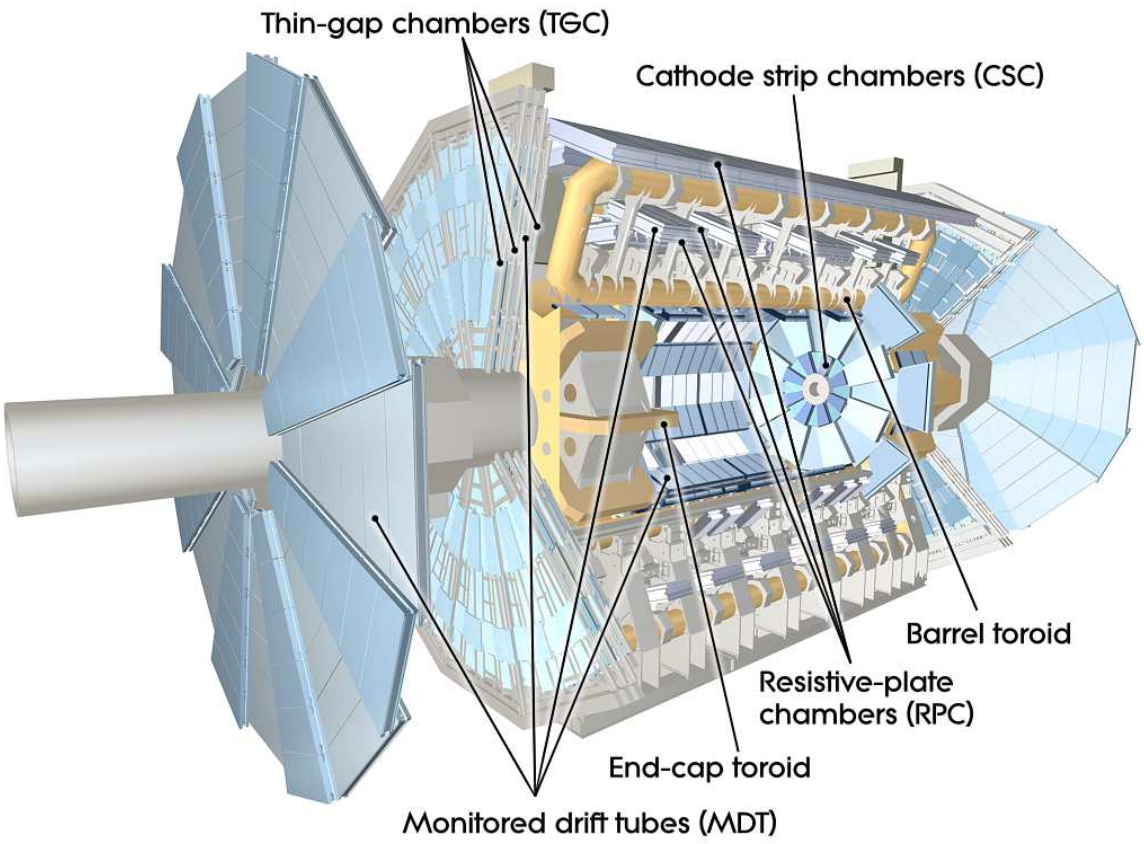

Figure 2.5: The ATLAS muon spectrometer.

2.4.1 Monitored Drift Tube Chambers

MDT chambers contain 29.970 mm diameter aluminum drift tubes, filled with a 97%:3% mixture of Ar:CO_2 gasses held at a pressure of 3 bar. Each tube is coaxial with a tungsten-rhenium anode wire operated at HV$\sim$3080 V. When a charged particle (which, having penetrated the calorimeter system, is presumably a muon) passes through a tube, it ionizes the gas. The resulting electrons drift towards the anode wire, producing (up to 700 ns later) a current that registers a physics hit. The distance of the hit from the sense wire is measured based on the time delay between the bunch crossing and detection of the hit. Each MDT chamber used in the ATLAS MS consists of two sets of layers, called multilayers, one on either side of an aluminum frame, each composed of four (three) layers of MDTs if part of the innermost (other two) precision layers of the MS. The MDT are all oriented along the azimuthal direction, allowing for a precise measurement of the η coordinate of each hit.

2.4.2 Cathode Strip Chambers

CSCs are multi-wire proportional chambers, composed of four planes, each constructed as a plane of parallel gold-plated tungsten-rhenium anode wires, spaced 2.5 mm apart, biased at HV∼1900 V, and sandwiched between two layers of copper cathode strips, one parallel and the other perpendicular to the wires, both 2.5 mm from the wires. The space between the cathode strips is filled with an 80%:20% mixture of Ar:CO_2 gasses. When a charged particle passes through a chamber, it ionizes the gas, allowing a current to flow across the electrodes, resulting in a charge accumulating on both sets of cathodes. The ϕ (η) coordinate of a hit is measured based on the relative proportions of charge accumulated on 3-5 adjacent parallel (perpendicular) strips. Each endcap is composed of sixteen chambers, eight large (containing 1.519 mm wide perpendicular strips, 21.00 mm wide parallel strips, and 402 anode wires) and eight small (containing 1.602 mm wide parallel strips, 12.52 mm wide perpendicular strips, and 250 anode wires), all oriented so that the central wire is in the radial direction.

2.4.3 Resistive Plate Chambers

RPCs are composed of two detectors, each composed of two layers. Each layer is constructed from a pair of parallel phenolic-melminic plastic laminate electrode plates, separated by a 2 mm gas gap. The gas gap is filled with a 94.7%:5%:0.3% mixture of $C_2H_2F_4$:Iso-C_4H_{10}:SF_6. The plastic electrode plates are coated with a layer of graphite paint, and then glued to a PET film laminated with copper pick-up strips that are separated from copper ground plates by polystyrene pads and oriented azimuthally on one side of the gas volume and longitudinally on the other to enable measurements of both the η and ϕ coordinates of tracks. The layers are interleaved with paper honeycomb support panels. The plastic electrodes are biased at HV∼9.8 kV, so when a charged particle passes through a gas volume, it ionizes the gas and produces a current that flows into the pick-up strips and registers a physics hit.

2.4.4 Thin Gap Chambers

TGCs are multi-wire proportional chambers, composed of two (three, in the case of the station associated with the middle precision layer) layer stations. Each layer is constructed using a pair of FR4 plates, separated by a 2.8 mm cavity. The plates are coated with a layer of graphite cathode on the inside and mounted with copper pick-up strips (pick-up plates for the middle layer when there are three) on the outside. The layers are separated by layers of honeycomb paper. Inside the cavities, there are parallel gold-coated tungsten anode wires, separated by 1.4 mm and biased at HV∼2.9 kV. The cavity is filled with a 55%:45% mixture of CO_2-C_5H_{12} gas. The pick-up strips are oriented radially, to allow for

measurement of the ϕ coordinate of hits, to compliment the η measurements of the MDT, and the chambers are segmented radially to allow for independent η measurements. When a charged particle passes through a layer, it ionizes the gas, which, due to the very strong electric field, produces an avalanche of electrons that flow between the pick-up strips/plates and the wires as detectable currents. The ϕ coordinate of the hit is measured based on the distribution of the current in multiple adjacent strips, and the η coordinate is measured based on the current through the wires in multiple adjacent layers of chambers.

2.5 ATLAS Magnets

The ATLAS magnet system consists of a solenoid surrounding the inner detector and a toroid (for which the ATLAS detector is named) surrounded by the muon spectrometer. The magnet windings are shown in Figure 2.6.

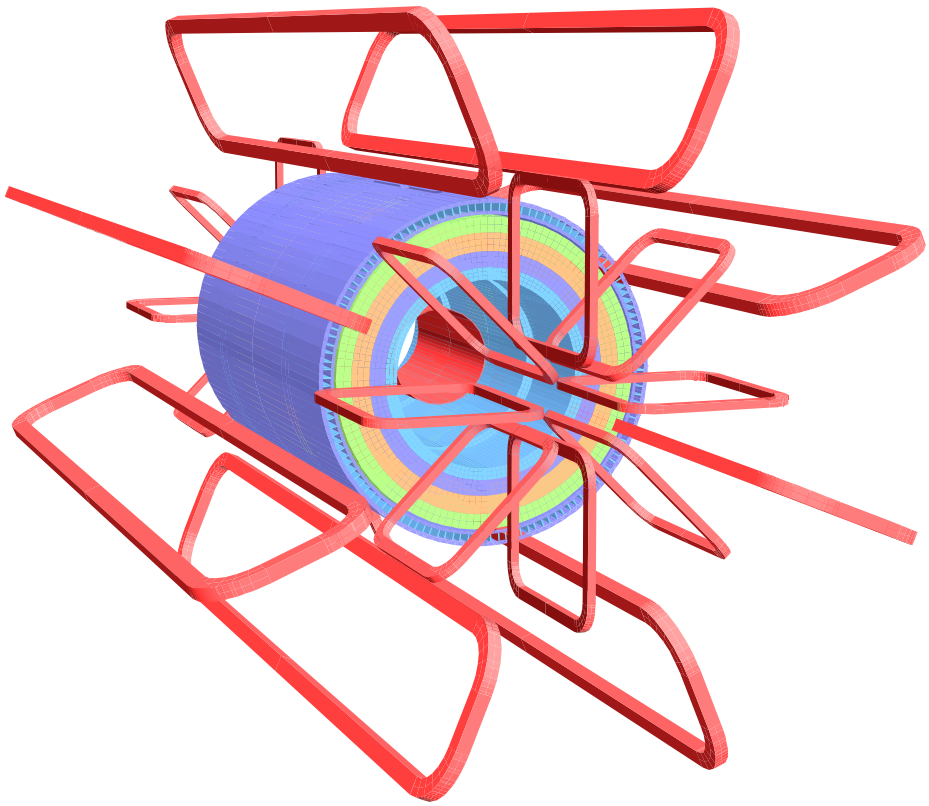

Figure 2.6: The ATLAS magnets. The windings of the solenoid and toroid are shown in red and the ferromagnetic parts of the tile calorimeter are shown in various colors.

2.5.1 Solenoid Magnet

The solenoid magnet is made of a single layer of aluminum-stabilized niobium-titanium conductor, wound inside of an aluminum superstructure that surrounds the ID package. The magnet is electrified at 7.73 kA and produces a local magnetic field of ∼2 T. It is used to bend the paths of charged particles in ϕ, keeping η approximately constant, as they propagate through the ID to allow for measurements of their charge-to-momentum ratios ($\frac{q}{p}$) based on their curvature in the known magnetic field.

2.5.2 Toroid Magnet

The toroid magned is made of an aluminum-stabilized niobium-titanium-copper conductor, wound around an aluminum superstructure that lies between the inner and middle layers of the MS in both the barrel and endcaps, as well as between the middle and outer layers of the MS in the barrel only. The magnet is electrified at 20.4 kA and produces an ambient magnetic field of ∼0.5 (1.0) T in the barrel (endcaps). It is used to bend the paths of charged particles in η, keeping ϕ approximately constant, as they propagate through the MS to allow for measurements of their $\frac{q}{p}$ based on their curvature in the known magnetic field.

Chapter 3
Trigger & Data Acquisition

The 50 ns spacing between bunches of protons translates into a 20 MHz collision rate. Given the magnitude of data produced by such a complex detector, reading out every collision would be infeasible. As such, ATLAS has a multi-stage trigger & data acquisition (TDAQ) system that chooses potentially interesting events and records relevant information. The trigger portion of the system consists of three levels of trigger systems managed by a computer system called the central trigger processor (CTP): level one (L1) hardware triggers that reduce the event rate to ∼50 kHz plus level two (L2) and event filters (EFs) software triggers that further reduce the event rate to a manageable level (∼500 Hz). The data acquisition (DAQ) portion of the system includes computer systems called read out drivers (RODs) and read out systems (ROSs) for each detector subsystem, as well as central computer systems called the region of interest builder (RoIB) and the event builder (EB), and a dedicated set of storage elements on the CERN CASTOR disk server. The data sample studied in this analysis was selected using high-p_{T} single-lepton algorithms, allowing either an electron or a muon to trigger the acquisition of each event.

3.1 Data Acquisition

When one of the L1 trigger systems indicates that a collision produced a potentially interesting physics signature (e.g., a high-p_{T} lepton), a command is sent from the CTP to the detector to read out hits and energy deposits. These data are sent via RODs to ROSs, each of which combines the data from a few RODs into an event fragment. The CTP forwards the L1 decisions to the RoIB, which identifies the portion of the detector in the direction (w.r.t. the IP) of the object that satisfied the L1 trigger as a region of interest (RoI). The event fragments corresponding to the RoIs are sent to the L2 computing cluster, which returns a trigger decision for each algorithm enabled during the run that is seeded by (i.e., that corresponds to) a L1 algorithm satisfied in the event. If a L2 algorithm is satisfied, all fragments from the event are collected from the ROSs by the EB, which assembles the

event record and sends it to the EF computing cluster, which returns a trigger decision for each EF algorithm enabled during the run that is seeded by a L2 algorithm satisfied in the event. If an EF algorithm is satisfied, the event record is written to a storage element on CASTOR. This event record, consisting of hits and energy deposits, as well as the details of all of the physics objects reconstructed by the triggers, is stored in a root file in a format called raw data output (RDO). Additionally, the state of the detector (i.e. information for each part of the detector regarding what was powered and enabled for data-taking) is written to a conditions database, which is then used when reconstructing the event offline.

3.2 Electron Trigger

3.2.1 L1

The L1 trigger algorithm used to select events containing high-p_{T} electrons checks for the presence of substantial energy deposits in the EM calorimeter. To accomodate the read-out bandwidth constraints imposed by the 20 MHz collision rate, the trigger functions by summing over all of the energy deposits in each trigger tower (a set of cells spanning all three layers radially and 0.1×0.0982 in $\eta - \phi$ space) within the calorimeter before reading out the total energy deposit for each bunch crossing and comparing it to an energy threshold. In this analysis, the energy threshold used was 14 GeV, and the algorithm used is denoted L1_EM14. As the LHC ramped up the number of bunches in the filling scheme, the increased collision rate eventually required a more selective algorithm. To maintain a manageable trigger rate, a new algorithm was introduced with a higher energy threshold (30 GeV), denoted L1_EM30. In addition, a modified algorithm was introduced, which preserves acceptance of events with electrons by keeping the 14 GeV threshold but requires that the trigger towers in the hadronic calorimeters corresponding to the tower that would fire the L1_EM14 trigger have no more than 1 GeV total energy deposited in the event, as electrons are almost always absorbed by the EM calorimeter. This modified algorithm is denoted L1_EM14VH, where the VH indicates the requirement on hadronic energy (V_h). Since the requirement on hadronic energy is not calculated relative to the energy of the cluster, very high energy (i.e. $p_{\mathrm{T}} \gtrsim 300$ GeV) electrons can be rejected; to mitigate this inefficiency, when the VH algorithm was introduced, it was taken as a logical OR with L1_EM30.

3.2.2 L2

The L2 electron trigger algorithm used in this analysis reconstructs electrons by first reconstructing ID tracks as in Section 4.1.1 and EM clusters as in Section 4.2.1. It then matches tracks to clusters to reconstruct electrons as in Section 5.1, and requires that the tracks be well reconstructed, that the clusters have energy distributions between cells that are

consistent with electrons (which, unlike photons, do not first need to convert to electron-positron pairs to deposit energy in the EM calorimeter, and are consequently more likely to deposit energy in the first layer), and that the track momentum match the cluster energy. The electrons in the RoIs sent to the L2 system are each tested against the trigger hypothesis (viz. that there is a high-p_{T} electron in the event). Due to the aforementioned increasing collision rates, the L2 trigger hypothesis in use for this analysis was modified for all data collected after July 2011 from defining a high-p_{T} electron as having $p_{\mathrm{T}} > 20$ GeV (denoted L2_e20_medium) to 22 GeV (denoted L2_e22_medium). Additionally, when the L1 trigger algorithm was changed from L1_EM14 to L1_EM14VH, the requirements on the cluster shape in the electron selection were relaxed somewhat, while the requirements on the tracks quality were tighened, resulting in a further modified trigger algorithm (denoted L2_e22vh_medium1). Also, when the non-VH 30 GeV algorithm was introduced to mitigate the inefficiency at high energy of the VH algorithm, a new L2 algorithm was created seeded by it (denoted L2_e45_medium1), which used the same modifed track and cluster requirements as L2_e22vh_medium1. As at L1, the logical OR of the two algorithms was taken at L2.

3.2.3 EF

The EF electron trigger algorithm used in this analysis reconstructs and selects electrons by the same method as the L2 algorithm, only it uses the hits and energy deposits from the detector, not only the RoIs. This results in an EF algorithm corresponding to each L2 algorithm, all denoted by simply replacing the "L2" in the name with "EF". As at L1 and L2, the logical OR with the non-VH algorithm was taken when the VH trigger was implemented. The electron EF triggers used in this analysis are listed in Table 3.1.

Dates	LHC Fills	Electron Trigger	Muon Trigger
April 14 - July 29	1711-1991	EF_e20_medium	EF_mu18_MG
July 30 - August 4	1992-2001		EF_mu18_MG_medium
August 4 - August 22	2005-2040	EF_e22_medium	
September 7 - October 30	2083-2267	EF_e22vh_medium1 OR EF_e45_medium1	

Table 3.1: Triggers used for various parts of the 2011 proton-proton collision run to select the data sample for this analysis.

3.3 Muon Trigger

3.3.1 L1

The L1 trigger algorithm used to select events containing high-p_{T} muons checks for coincidences of track segments reconstructed at multiple stations in the MS along a path with approximately constant $\frac{q}{p}$ through the toroid field. To accomodate the read-out bandwidth constrains imposed by the 20 MHz collision rate, the trigger functions by reading out hits in the RPCs and TGCs, in a coarse resolution. The hits are then used to reconstruct individual segments at each station. The trigger requirement used in this analysis is that the $\frac{q}{p}$ of the path through the toroid field be consistent with a muon of $p_{\mathrm{T}} > 10$ GeV (denoted L1_MU10). As the LHC increased the collision rate, the momentum threshold used in this analysis was increased to 11 GeV (denoted L1_MU11).

3.3.2 L2

The L2 muon trigger algorithm used in this analysis reconstructs muons in each RoI by first reconstructing ID tracks as in Section 4.1.1 and MS tracks as in Section 4.3.2. It then combines the ID and MS tracks as in Section 5.2. The muons in the RoIs sent to the L2 system are each tested against the trigger hypothesis (viz. that there is a high-p_{T} muon in the event). The trigger hypothesis in use for this analysis defines a high-p_{T} muon as having $p_{\mathrm{T}} > 18$ GeV (denoted L2_mu18_MG). When the L1 trigger seeding the L2 algorithm was changed from L1_MU10 to L1_MU11, the L2 requirements were kept the same, but the algorithm was renamed L2_mu18_MG_medium.

3.3.3 EF

The EF muon trigger algorithm used in this analysis reconstructs muons by the same method as the L2 algorithm, only it uses the hits from the detector, not only the RoIs. This results in an EF algorithm corresponding to each L2 algorithm, all denoted by simply replacing the "L2" in the name with "EF". The muon EF triggers used in this analysis are listed in Table 3.1.

Chapter 4
Event Reconstruction

Each recorded event is reconstructed by the ATLAS Tier0 computing cluster at CERN. The hits and energy deposits recorded by the three main systems of the detector are used to reconstruct detector objects: ID tracks/vertices/conversions, calorimeter clusters, and MS tracks/segments. These detector objects are then used to reconstruct physics objects (as discussed in Chap. 5). This process is first conducted on a subset of the data from a given fill, using a reference set of assumptions about the detector and beam geometry/state. The resulting detector and physics objects are used both to determine the actual conditions during data-taking (e.g. the alignment of the MS w.r.t. the ID) and to evaluate the quality of the data acquired (which is used to select events as described in Section 7.1). Once the conditions have been determined, the reconstruction is repeated, this time on all events recorded in the fill. The output of the reconstruction process is written to disk in the event summary data (ESD) format, which is then reprocessed twice, each time calculating additional properties of the reconstructed objects, finally resulting in data written to disk in the thrice derived physics data (D3PD) format.

4.1 Inner Detector

Charged particle tracks traversing the ID are reconstructed from the hits recorded by the three tracking subsystems. The tracks are then used to reconstruct vertices from which the tracks are assumed to have originated [11]. The remaining hits that were not used to reconstruct tracks are then used to reconstruct secondary tracks, that are used to identify conversions, wherein photons are absorbed by detector material which then emits electron-positron pairs.

4.1.1 Tracks

The tracking algorithm used by ATLAS first takes the hits in the pixel detector, as well as the first layer of the SCT, and forms track seeds from combinations of hits, requiring at

least three hits per track seed. The track seeds are then used to form track candidates, by extending their paths through the SCT and adding SCT hits consistent with the extensions. The track candidates are then fit to helical paths through the solenoid field, assuming the pion hypothesis (i.e. unit charge and pion mass). The resulting silicon tracks are then extrapolated into the TRT. The TRT hits are then assigned to the extensions of silicon tracks based on proximity. Finally, all of the hits (silicon and TRT) associated with each silicon track are fit together into a single helical path through the entire ID volume, which is called an ID track. Any TRT hits whose inclusion reduces the quality of the ID track fit relative to the silicon track fit are classified as outliers, and excluded from the ID track fit.

4.1.2 Vertices

The vertexing algorithm used by ATLAS starts by extrapolating all tracks in an event to the beam line. Starting with the track closest to the nominal IP, tracks are combined into a vertex based on a χ^2 fit to the hypothesis that all associated tracks originated at the vertex. Tracks located at increasing distance from the first vertex are added until a track is found to be 7σ from the vertex. That track is then used to seed a new vertex, and the process is repeated. Once all tracks have been thus assigned, the vertex in the event with the highest value of $\sum_{\text{tracks}} p_{\text{T}}^2$ is denoted the primary vertex (PV).

4.1.3 Conversions

The TRT hits that were not associated with any tracks are reconstructed into secondary track segments. The segments are then extrapolated back through the SCT and pixel detectors, and silicon hits that were not associated with any tracks are added to produce secondary track candidates, that are then fit to helical paths through the ID volume called secondary tracks. Conversion candidates are identified as the points within the ID whence secondary tracks originate.

4.2 Calorimeters

The shower of a particle in the calorimeters is typically wider than a single cell, so the deposition of energy in adjacent cells are grouped together into a cluster. Two types of calorimeter clusters are used in this analysis: clusters reconstructed using the sliding-window algorithm solely using the EM calorimeter, called EM clusters, and clusters reconstructed using the topological algorithm using all of the calorimeters, called topological clusters or topoclusters [12].

4.2.1 Electromagnetic Clusters

The EM cluster reconstruction algorithm used in this analysis first divides the EM calorimeter into a grid in $\eta - \phi$ space with cell size 0.025×0.025. It then scans through the grid with a 5 cell×5 cell (0.125×0.125 in $\Delta\eta \times \Delta\phi$) window to find preclusters, which are regions wherein the total deposition has transverse energy[2] $E_{\mathrm{T}} > 3$ GeV. The location of the precluster is determined by finding the energy-weighted barycenter of the cells within a smaller position finding window (3 cell×3 cell) concentric with the larger window. From each precluster, an EM cluster is then defined as the set of cells within a cluster window centered at the precluster position. The cluster window used in this analysis is 3 cell×7 cell for electrons/converted photons in the barrel, 3 cell×5 cell for unconverted photons in the barrel, and 5 cell×5 cell for all particle types in the endcap.

4.2.2 Topological Clusters

The topocluster reconstruction algorithm used in this analysis first scans through all cells in the calorimeters to find proto-clusters, defined as clusters with signal-to-noise ratio of at least 4, where the signal is the absolute value of the measured cell energy and the noise is the electronic noise added in quadrature with the expected effect of pile-up interactions (i.e. additional interactions in the same or previous bunch crossing). Beginning with the proto-cluster that has the highest signal-to-noise ratio, each is enlarged by adding all adjacent cells with non-zero energy. After this procedure, each proto-cluster is again enlarged by adding cells adjacent to any cell with signal-to-noise ratio of at least 2. This process is iterated until there are no more cells at the edge of a proto-cluster with signal-to-noise of at least 2. Proto-clusters are merged if they grow to be adjacent, and those that remain after the iterative process are denoted clusters. Since there is no explicit limit on the size of clusters, they can grow to contain the showers of multiple nearby particles. As such, a cluster with ≥ 4 cells is split into smaller clusters if there are local maxima within the cluster. In that case, the cluster is split into a separate cluster for each local maximum, by repeating the clustering algorithm within the parent cluster and without proto-cluster merging, starting from only the cells with local maxima as the initial proto-clusters. The resulting split or single maximum clusters are defined as topoclusters.

4.3 Muon Spectrometer

Charged particle track segments through each of the three layers of the MS are reconstructed using hits in both the precision layers and the trigger chambers. The resulting segments are then combined into MS tracks when possible [13].

[2]Calculated assuming the energy is deposited by a particle originating at the nominal IP.

4.3.1 Track Segments

The algorithm used to reconstruct MS track segments first looks in each station (including the precision layers associated thereto) and fits the hits for the given event into a straight line (assuming minimal deflection in the toroid field over the length of the station). The segments are required to originate near the IP. When there are no trigger chamber hits to provide ϕ measurements to complement the η measurements of the MDT, the ϕ position of the center of the MDT chamber is used.

4.3.2 Muon Tracks

A particle originating near the IP that penetrates the calorimeters and traverses the MS is typically detected by multiple stations, so muon tracks are constructed by fitting together segments from multiple stations along paths through the toroid field, assuming the muon hypothesis (i.e. unit charge and muon mass). When reconstructing physics objects, two categories of MS objects are used, tracks and track segments, excluding the segments used to construct MS tracks.

Chapter 5
Physics Object Reconstruction

The ID tracks/vertices/conversions, calorimeter clusters, and MS tracks/segments can be used to reconstruct various physics objects: leptons (e, μ, τ), photons, jets, and $E_{\mathrm{T}}^{\mathrm{miss}}$.

5.1 Electrons

An electron is identified by matching an ID track to an EM cluster, based on both physical proximity and cluster energy-track momentum consistency [14]. The 4-momenta of the resulting electrons used in this analysis are determined by using the calorimeter energy measurement and the ID track direction.

5.2 Muons

Due to their higher mass, muons are less likely to interact with the calorimeter than electrons and much more likely to penetrate to the MS. As such, muons are reconstructed using ID tracks in conjunction with MS tracks/segments. Two types of muons are used in this analysis: combined, reconstructed by fitting the extrapolations of MS tracks back to the IP with matching ID tracks, and segment-tagged, reconstructed by finding MS track segments that match the extrapolations of ID tracks into the MS [13]. The segment-tagged muons are only used to reconstruct Z-bosons for offline analysis, while combined muons are used both in the trigger and to reconstruct the W- and Z-bosons in the offline analysis.

5.3 Taus

The hadronic decay of a τ-lepton typically produces one or three charged hadrons, all of which leave tracks in the ID and deposit energy in the calorimeters. As such, τ-leptons are reconstructed from EM clusters that match sets of either one or three ID tracks. Several multi-variate techniques are used to optimize the reconstruction. The visible energy of a

τ-lepton candidate is calculated as the total energy deposited in all cells with $\Delta R < 0.2$ w.r.t. the candidate.

5.4 Photons

An EM cluster is classified as a photon if it does not match any ID track and its shower shape is consistent with a photon. However, a photon could undergo conversion to an electron-positron pair, which will leave tracks in the ID. To reconstruct converted photons, EM clusters consistent with electrons are identified that match to reconstructed conversions.

5.5 Jets

Hadronic jets are reconstructed from topoclusters using the anti-k_t algorithm with a radius parameter $R = 0.4$ [15], which considers each topocluster with $E_{\mathrm{T}} > 7$ GeV. It calculates "distance" parameters for the i^{th} topocluster (or combination of topoclusters) as:

$$d_{ij} = min\left[\frac{1}{p^2_{\mathrm{T}i}}, \frac{1}{p^2_{\mathrm{T}j}}\right] \times \frac{(\Delta R_{ij})^2}{R^2}, \tag{5.1}$$

$$d_{iB} = \frac{1}{p^2_{\mathrm{T}i}}, \tag{5.2}$$

relative to the j^{th} topocluster (or combination of topoclusters) that has not yet been assigned to a jet. If $d_{iB} < d_{ij}$, the i^{th} object is determined to be a jet; otherwise, objects i and j are combined into a single object. This process is repeated until all topoclusters with $E_{\mathrm{T}} > 7$ GeV have been assigned to a jet.

5.6 Missing Transverse Energy

Missing transverse energy is defined as the imbalance of energy-momentum reconstructed in the event, and is assumed to originate from neutrinos produced in the event escaping undetected. It is calculated from all other reconstructed objects in the event as:

$$\begin{aligned} E_{\mathrm{T}}^{\mathrm{miss}} = & -\sum_{e} \mathbf{p}_{\mathrm{T}}(e_i) - \sum_{\mu} \mathbf{p}_{\mathrm{T}}(\mu_i) - \sum_{\tau} \mathbf{p}_{\mathrm{T}}(\tau_i) - \sum_{\gamma} \mathbf{p}_{\mathrm{T}}(\gamma_i) - \sum_{j} \mathbf{p}_{\mathrm{T}}(j_i) \\ & - \sum_{\text{soft tracks}} \mathbf{p}_{\mathrm{T}}(trk_i) - \sum_{\text{topoclusters}} \mathbf{p}_{\mathrm{T}}(cl_i), \end{aligned} \tag{5.3}$$

where soft tracks are those with $p_{\mathrm{T}} < 10$ GeV. To avoid double counting, the soft tracks and topoclusters in the formula include only those objects not used to reconstruct any of the physics objects [16].

Chapter 6
Monte Carlo

The theoretical predictions tested by this analysis are translated from Lagrangian terms into an expected event yield and kinematic distributions by Monte Carlo (MC) simulation. The simulation process proceeds in two main steps: simulation of the physics processes involved in $W^{\pm}Z$ production in proton collisions and simulation of the detector response to the various particles produced by the physics simulation [17].

6.1 Physics Simulation

The simulation of the physics processes involved in $W^{\pm}Z$ production is performed in five stages: the structure of the incident protons, the matrix element (ME) of the hard scattering process, the underlying event (UE), the parton shower (PS) and hadronization, and various processes not well modeled by the preceeding simulations.

6.1.1 Parton Distribution Function

As described in Section 1.1.2, the proton is a composite particle, whose various constituent partons participate in $W^{\pm}Z$ production. As such, before simulating the production process, one must first simulate the incident protons. In this analysis, the incident protons are modeled using the CT10 parton distribution function (PDF) set [18].

6.1.2 Matrix Element

Starting from the partons supplied by the PDF, the hard scattering interactions resulting in $W^{\pm}Z$ production are simulated using the MC@NLO generator [19, 20], which performs a next-to leading order (NLO) calculation of the process and simulates the leptonic decays of the resulting bosons. For each of the nine decay channels studied in this analysis ($\{W \to e/\mu/\tau\} \otimes \{Z \to e/\mu/\tau\}$), a sample of ~50000 events was generated.

6.1.3 Underlying Event

To model the evolution of all partons from the incident protons other than those involved in the hard scattering process, the auxiliary UE modeling program JIMMY is used [21].

6.1.4 Parton Shower & Hadronization

Once the scattering has been simulated and all incident partons have been converted into out-going partons, the transformation of those partons into stable particles that can then be detected is modeled by the PS generator HERWIG [22]. Additionally, HERWIG models the QCD initial state radiation (ISR) and final state radiation (FSR); the formation of stable hadrons from the unstable, strongly interacting out-going partons; the quantum electrodynamic (QED) ISR; and the soft ($E_{\mathrm{T}} < 20$ GeV) QED FSR of out-going charged partons (especially the charged leptons produced in vector boson decays).

6.1.5 Special Generators

Certain parts of the PS process are not well modeled by HERWIG. Special generators are used in this analysis for two such parts: τ-lepton decays and hard ($E_{\mathrm{T}} > 20$ GeV) QED FSR. The τ-lepton decays are modeled using the TAUOLA program [23], and the hard QED FSR is modeled by the PHOTOS program [24].

6.2 Detector Simulation

The interaction of stable particles, produced by the PS simulation, with the ATLAS detector is modeled using the GEANT4 simulation program [25]. The simulation uses typical detector conditions during data-taking. It takes the stable particles from the physics simulation and propagates each through the detector, simulating its interactions with each encountered element thereof. The simulated response of the detector to the particles in the event are then digitized into hits and energy deposits, whose effects on the trigger systems are also simulated. The resulting event record is then written to disk in the RDO format, including the records of the simulation process. These MC RDO files are then reconstructed using the same procedure as the real data, and processed into D3PD format in the same way, including the record of the simulation.

6.3 Pile-up

Since the response of the calorimeters takes more than 50 ns, the energy depositions in a particular bunch crossing affect the calorimeter response in several succeeding bunch crossing. This effect and the effects of multiple interactions in a single bunch crossing are

simulated assuming that the typical hard scattering process in the interactions is a QCD di-jet or multi-jet interaction, wherein strongly interacting incident partons produce strongly interacting out-going partons. These interactions are simulated using the PYTHIA [26] generator, with the CTEQ6L1 [27] PDF set as inputs, for all steps except τ-lepton decays and hard QED FSR, which are simulated per Section 6.1.5.

6.4 aTGC Samples

In order to set limits on aTGC, $W^{\pm}Z$ production must be simulated as a function of the couplings. This is accomplished by the use of a set of nine samples, of ∼50000 events each, generated at a particular anomalous coupling point and then reweighted to arbitrary couplings. The three terms in the aTGC Lagrangian (Equation 1.1) produce nine anomalous terms in the scattering cross section. The contribution of a particular simulated event to each of those terms can be quantified by a set of 10 weights (1 SM+9 aTGC), and the total weight of an event can be expressed as a function of the couplings, as:

$$\begin{aligned} w \;\propto\; w_0 \;&+ \left(\Delta g_1^Z\right)^2 w_1 + \left(\Delta\kappa^Z\right)^2 w_2 + \left(\lambda^Z\right)^2 w_3 \\ &+ 2\Delta g_1^Z w_4 + 2\Delta\kappa^Z w_5 + 2\lambda^Z w_6 \\ &+ 2\Delta g_1^Z \Delta\kappa^Z w_7 + 2\Delta g_1^Z \lambda^Z w_8 + 2\Delta\kappa^Z \lambda^Z w_9, \end{aligned} \tag{6.1}$$

where the weight of each event has a relative phase of ± 1, w_0 is the weight of the event contributing to SM production, and the other w_i are the weights for the nine anomalous cross section terms. The sample is reweighted by varying the weight of each event per Equation 6.1 [20].

6.5 MC Normalization

The $W^{\pm}Z$ simulations for both SM and aTGC couplings are normalized using the NLO cross sections, calculated with MCFM [28], to the total integrated luminosity (4.64 fb^{-1}), per Section 2.2.4.

6.6 Background MC

In addition to the signal MC, several physics processes that produce background to the trilepton+large $E_{\mathrm{T}}^{\mathrm{miss}}$ signature are simulated using several generators, including those aforementioned plus ALPGEN [29], MADGRAPH [30], and SHERPA [31], using the aforementioned PDF sets plus MRST [32]. All background samples use the same pile-up modeling and detector simulation, as well as the auxiliary MC programs TAUOLA and PHOTOS. The samples are listed, along with the parameters of their physics simulation and references for

their normalization cross sections, in Table 6.1. Although the central value of the $Z+$jets background is estimated from data, the systematic uncertainty in the extrapolation from low- to high-$E_{\mathrm{T}}^{\mathrm{miss}}$ is evaluated using simulation, the details of which are given in the table.

Process	PDF	ME	UE	PS	Normalization Reference
ZZ	MRST-MCal		Pythia		[28]
$Z\gamma$	CTEQ6L1		Sherpa		[28]
$t\bar{t}$	CT10	MC@NLO	Jimmy	Herwig	[33]
$t\bar{t}V$	CTEQ6L1	MadGraph	Pythia		[34, 35]
$Z+$jets	CTEQ6L1	Alpgen	Jimmy	Herwig	[36, 37]
W^+W^-	MRST		Herwig		[28]

Table 6.1: Details of the MC simulation of background processes.

Chapter 7
Event Selection

A number of criteria are used to select $W^{\pm}Z \to \ell^{\pm}\nu_{\ell}\ell'^{+}\ell'^{-}$ candidate events. First, events are required to have a minimum level of data quality (DQ). Then, the prompt electrons and muons to be used to reconstruct the vector boson candidates are required to have properties that distinguish them from converted photons, hadrons, and hadronic decay products. Finally, the $W^{\pm}Z$ candidates are selected by reconstructing the W- and Z-bosons using the selected leptons and $E_{\mathrm{T}}^{\mathrm{miss}}$. The simulated expectation of the number of $W^{\pm}Z$ events passing each step of the event selection is given in Table 7.1. The first part of the table excludes the tauonic decay channels, which are given on the last line. The efficiency corrections are discussed in Section 9.1.5.

	eee	μee	$e\mu\mu$	$\mu\mu\mu$
Produced		1202		
Muon or electron trigger		1121		
Primary vertex		1118		
$E_{\mathrm{T}}^{\mathrm{miss}}$ cleaning		1116		
Two leptons, $m_{\ell\ell}$	219		317	
Three leptons, p_{T}	51.2	70.6	74.8	106.6
$E_{\mathrm{T}}^{\mathrm{miss}} > 25\,\mathrm{GeV}$	40.5	57.0	59.2	86.4
$m_{\mathrm{T}}^{W} > 20\,\mathrm{GeV}$	38.1	54.1	55.7	81.9
Trigger match	38.0	54.0	55.3	81.7
Efficiency corrections	37.2	51.8	54.2	78.3
$W^{\pm}Z \to \tau X$ contribution	1.7	2.3	2.4	3.4

Table 7.1: Expected signal yield at each step in the event selection for the four leptonic final states.

7.1 Data Quality Requirements

To ensure the reliability of the MC modeling of the detector response, each minute of data-taking is analyzed and events are only used if there are no problems in any detector subsystem sufficiently severe as to produce any problem with the reconstruction. To reject non-collision background, and to ensure the validity of the tracking and vertexing used for the electron and muon reconstruction and identification, it is required that the vertexing algorithm including the track-vertex association be successful. This is accomplished by requiring that the reconstructed PV in the event be associated with at least 3 tracks. To ensure the integrity of the $E_{\mathrm{T}}^{\mathrm{miss}}$ calculation, events are rejected if there was excessive calorimeter noise (i.e. a collection of noisy calorimeter cells clustered into a jet with $p_{\mathrm{T}} > 20$ GeV).

7.2 Electron Selection

Additional requirements are imposed on the electron candidates reconstructed per Section 5.1 to mitigate the contamination of the electron sample by mis-identified or non-prompt objects. These requirements are implemented in two steps: a standard quality and identification selection, followed by a special isolation and ID track impact parameter selection.

7.2.1 Standard Quality & Identification

A set of quality criteria are required on the electron candidates. Moreover, a set of standard identification criteria, called loose++, are required to be satisfied by all electrons used to reconstruct Z-bosons. A tighter set of identification criteria, called tight++, are also required to be satisfied by all electrons used to reconstruct W-bosons, since there is no applicable invariant mass constraint.

Quality

The electron quality criteria are based on the EM calorimeter status and performance. First, electrons must be reconstructed using clusters located in regions of the EM calorimeter without hardware problems. Then, since the performance of the detector in reconstructing low-p_{T} electrons is not well understood, electrons are required to have $p_{\mathrm{T}} > 15$ GeV. Finally, electrons must not be reconstructed using clusters in the transition region between the barrel and endcap EM calorimeters ($1.37 \leq |\eta| \leq 1.52$) or the outer edge of the endcap calorimeter ($|\eta| \geq 2.47$).

Loose++

The loose++ set of selection criteria identifies electrons based on the properties of the ID tracks and EM clusters, namely:

- ≥ 1 pixel hit (including outliers)
- ≥ 7 silicon (pixel+SCT) hits (including outliers)
- $\Delta\eta < 0.015$ between the track and cluster
- p_{T}- and η-dependent requirements on several parameters of the calorimeter shower shape:
  - Width of energy deposition in the first layer
  - Width of energy deposition in the second layer
  - Narrowness in $\Delta\eta$ of entire energy deposition
  - Difference between the fractions of the energy deposited in the first and second layers, calculated as:
$$\delta \equiv \frac{E_{\text{Layer 1}} - E_{\text{Layer 2}}}{E_{\text{Layer 1}} + E_{\text{Layer 2}}} \tag{7.1}$$
- p_{T}- and η-dependent requirements on the fraction of energy deposited in the hadronic calorimeters

The $\Delta\eta$ requirement rejects coincidental matching of ID tracks and EM clusters from hadronic jets. The requirements on the width of the shower, both per layer and on the entire deposition, reject hadronic jets and decays of τ-leptons, since energy deposition by multiple nearby particles produces a wide shower. The requirement on the difference in energy deposits between calorimeter layers rejects coincidental matching of ID tracks with photons, since a photon is less likely to shower in the first layer of the calorimeter. The requirement on hadronic leakage rejects mis-identified hadrons, since electrons are unlikely to deposit significant energy in the hadronic calorimeters.

Tight++

The tight++ set of selection criteria identifies electrons based on several properties of the ID tracks and EM clusters, including tighter versions of all of the loose++ criteria. The additional criteria are:

- A test for conversions
- ≥ 1 b-layer hit (including outliers)

- ≥ 2 pixel hits (including outliers) if the track is in the endcap region
- η-dependent requirements on the number of TRT hits (including outliers)
- η-dependent requirements on the fraction of high-threshold TRT hits (including outliers)
- $\Delta\eta < 0.005$ between the track and cluster
- $\Delta\phi < 0.015$ between the track and cluster
- p_{T}- and η-dependent requirements on the ratio of track momentum to cluster energy
- $|d_0| < 1$ mm

As described in Section 2.2.3, the requirement on high-threshold TRT hits rejects charged hadrons. The additional track-cluster matching requirements further reject coincidental matching of ID tracks and EM clusters from hadronic jets. The requirement on the transverse impact parameter (d_0), defined as the distance of closest approach of the ID track to the beam axis (whereupon the PV is located) in the transverse direction, rejects non-prompt leptons from τ-lepton and heavy-flavor hadron decays, as well as conversions.

7.2.2 Isolation & Impact Parameter

The standard quality and identification requirements are effective for rejecting hadrons misidentified as electrons. They are also useful for rejecting some of the non-prompt electrons from conversions and heavy-flavor hadron decays. However, to mitigate contamination by non-prompt electrons remaining in the sample, additional electron quality criteria are required. Four such additional criteria are used in this analysis, regarding the electron properties: calorimeter isolation, ID track isolation, longitudinal impact parameter (z_0) of the ID track, and significance of the transverse impact parameter ($|d_0|/\sigma_{d_0}$) of the ID track.

Calorimeter Isolation

Since light-flavored hadrons and non-prompt electrons from heavy-flavor hadron decays are typically produced in jets that contain other particles, it is useful to evaluate the nearby activity when identifying prompt electrons from vector boson decays. This is accomplished by summing the energy of all calorimeter cells with $\Delta R < 0.30$ relative to the ID track of the electron. This energy, called Etcone30, is required to be $< 14\%$ of the electron p_{T}.

ID Track Isolation

Since some of the nearby activity in the jets that produce light-flavor hadrons and non-prompt electrons are charged, it can be useful to evaluate the nearby ID track activity as

well. This is accomplished by taking the scalar sum of the p_{T} of all $p_{\mathrm{T}} > 1$ GeV tracks associated with the PV in the event that have $\Delta R < 0.30$ relative to the ID track of the electron. This momentum, called ptcone30, is required to be $< 13\%$ of the electron p_{T}.

Longitudinal Impact Parameter

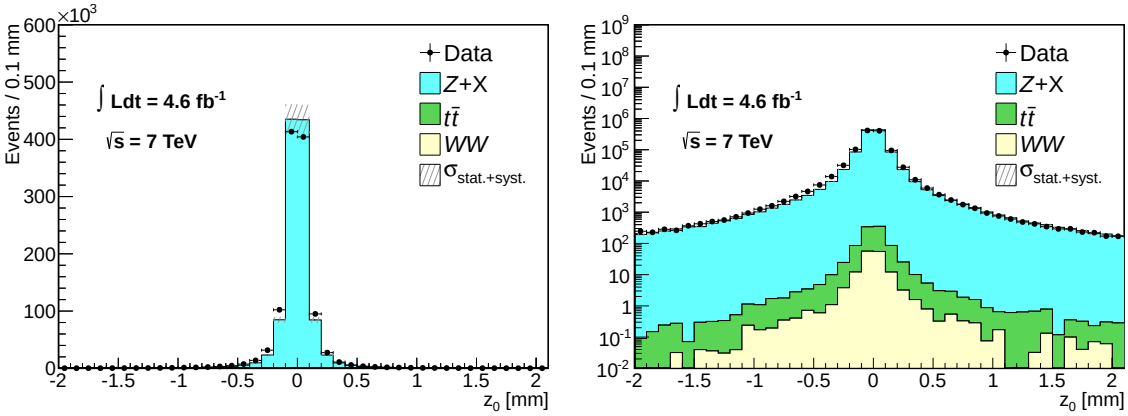

Figure 7.1: Comparison of the z_0 distribution of prompt electrons in data with simulation ($Z+$jets, $t\bar{t}$, and W^+W^-) in the Z-tagged control sample, in linear (left) and logarithmic (right) scale. The simulated expectation is normalized to the data.

To reject electrons produced in pile-up events, the ID track of the electron is required to be associated with the reconstructed PV in the event. To accomplish this, a requirement is imposed on the longitudinal impact parameter (z_0), defined as the z-coordinate of the point along the track closest to the beam axis. To determine an appropriate requirement, a sample of prompt electrons is evaluated using the Z Tag & Probe (T&P) method. The z_0 distribution (w.r.t the PV), in a control sample of events containing exactly two electrons and no muons and wherein the di-electron invariant mass is within 10 GeV of the Z-boson mass (91.1876 GeV [38]), is shown in Figure 7.1. To preserve high signal efficiency, the z_0 of electron candidates is required to be within 1 mm of the z-coordinate of the PV.

Transverse Impact Parameter Significance

Vector boson decays occur at the PV, whereas the photon conversions and heavy-flavor hadron decays that produce non-prompt electrons typically occur near or inside the ID. As such, contamination of the electron sample by such sources can be mitigated by imposing a requirement on the transverse distance from the PV at which the electron originated (d_0). This requirement is defined in units of the uncertianty (σ_{d_0}) in d_0, as $|d_0|/\sigma_{d_0}$. To determine

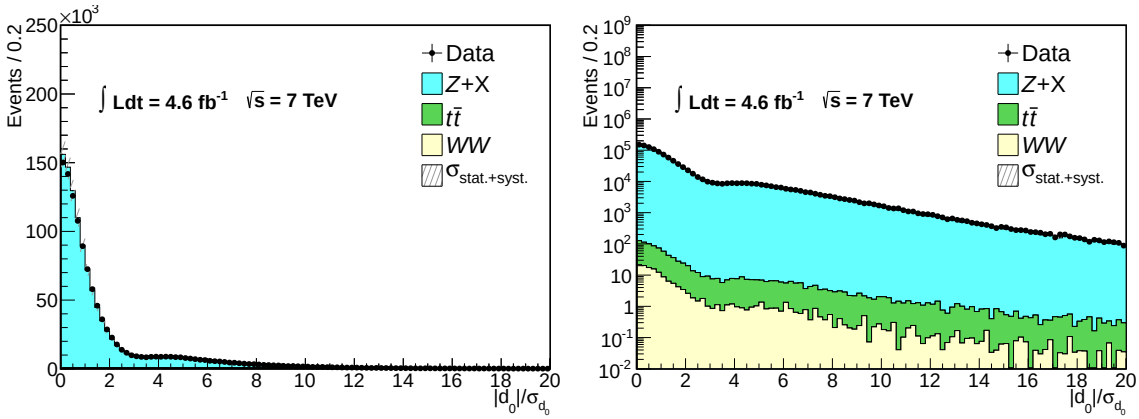

Figure 7.2: Comparison of the $|d_0|/\sigma_{d_0}$ distribution of prompt electrons in data with simulation (Z + jets, $t\bar{t}$, and W^+W^-) in the Z-tagged control sample, in linear (left) and logarithmic (right) scale. The simulated expectation is normalized to the data.

an appropriate requirement, the same Z-tagged electron sample is used. The $|d_0|/\sigma_{d_0}$ distribution of prompt electrons in the Z-tagged control sample is shown in Figure 7.2. To preserve high signal efficiency, the d_0 of electron candidates is required to be within ten standard deviations of the beam axis (i.e. $|d_0|/\sigma_{d_0} < 10$).

7.3 Muon Selection

A muon candidate is reconstructed (Section 5.2) by matching a charged particle in the ID to a charged particle in the MS. To reduce non-prompt muons produced in the decays of light-flavor (e.g. pions/Kaons) or heavy-flavor hadrons, two additional requirements are imposed: a standard quality selection and a special isolation and ID track impact parameter selection.

7.3.1 Quality

Since the performance of the detector in reconstructing low-p_{T} muons is not well understood, muons are required to have $p_{\mathrm{T}} > 15$ GeV. To ensure the integrity of the muon reconstruction, which is highly dependent on the ID tracking, and to reject muons from in-flight decays of light-flavor hadrons, which tend to occur in the vicinity of the TRT, when selecting the muons used in this analysis, a standard set of quality criteria are required of the ID tracks of the muons, namely:

- ≥ 1 hit in the b-layer
- ≥ 2 hits in the pixel detector

- ≥ 6 hits in the SCT
- < 3 layers of silicon (pixel+SCT) sensors traversed without registering a hit
- A successful TRT extension of the silicon track:
  - In the region of complete TRT coverage ($|\eta| < 1.9$): ≥ 6 TRT hits and outliers must be $< 90\%$ of hits+outliers
  - In the region of partial TRT coverage: whenever there are ≥ 6 TRT hits, outliers must be $< 90\%$ of hits+outliers

In all criteria, dead sensors are treated as hits to increase acceptance. All muons are required to be within the ID acceptance ($|\eta| < 2.5$).

7.3.2 Isolation & Impact Parameter

To mitigate the contamination of the muon sample by non-prompt muons from heavy-flavor hadron decays three additional muon quality criteria are required: ID track isolation, longitudinal impact parameter (z_0) of the ID track, and significance of the transverse impact parameter ($|d_0|/\sigma_{d_0}$) of the ID track.

ID Track Isolation

As in the case of electrons, the sources of non-prompt muons are typically produced in jets containing additional activity, so it is useful to evaluate such activity when identifying prompt muons from vector boson decays. However, muons seldom deposit significant energy in the EM calorimeter. Consequently, the detector response to such depositions are not well understood, so it is difficult to distinguish them from nearby calorimeter activity. As such, only nearby ID track activity is evaluated. In this case, ptcone30, calculated in the same way as for electrons, is required to be $< 15\%$ of the muon p_{T}.

Longitudinal Impact Parameter

To reject cosmic muons and muons produced in pile-up events, muon candidates are required to be associated with the reconstructed PV in the event. As in the case of electrons, this is accomplished by imposing a requirement on the z_0 of the ID track. To determine an appropriate requirement, a sample of prompt muons is evaluated using the Z T&P method. The z_0 distribution (w.r.t the PV), in a control sample of events containing exactly two muons and no electrons and wherein the di-muon invariant mass is within 10 GeV of the Z-boson mass, is shown in Figure 7.3. To preserve high signal efficiency, muon candidates are required to have z_0 within 1 mm of the z-coordinate of the PV.

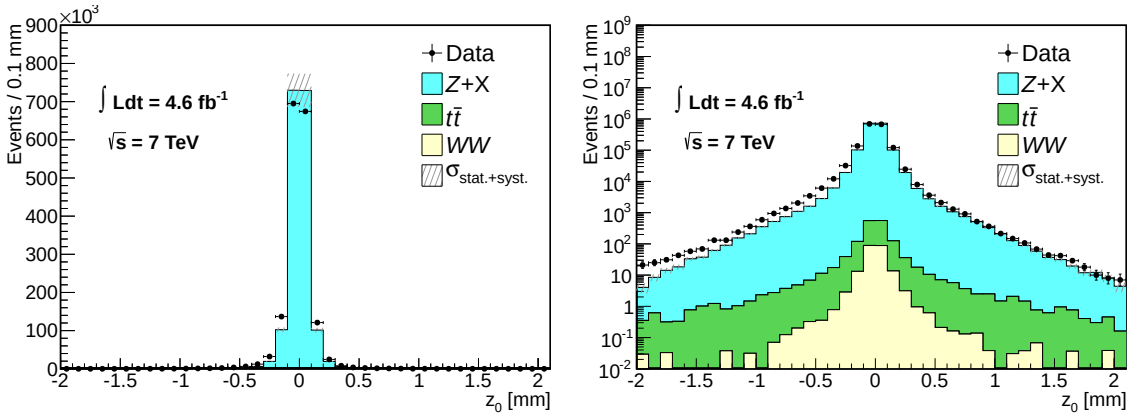

Figure 7.3: Comparison of the z_0 distribution of prompt muons in data with simulation ($Z+$jets, $t\bar{t}$, and W^+W^-) in the Z-tagged control sample, in linear (left) and logarithmic (right) scale. The simulated expectation is normalized to the data.

Transverse Impact Parameter Significance

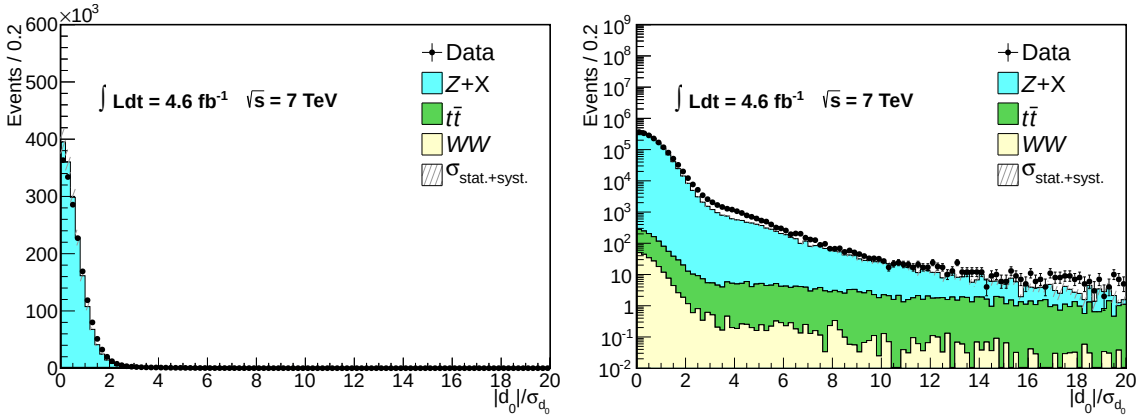

Figure 7.4: Comparison of the $|d_0|/\sigma_{d_0}$ distribution of prompt muons in data with simulation ($Z+$jets, $t\bar{t}$, and W^+W^-) in the Z-tagged control sample, in linear (left) and logarithmic (right) scale. The simulated expectation is normalized to the data.

Since, as in the case of electrons, vector boson decays occur at the PV, whereas the heavy-flavor hadron decays that produce non-prompt muons typically occur near or inside the ID, contamination of the muon sample by non-prompt muons can be mitigated by imposing a requirement on $|d_0|/\sigma_{d_0}$. To determine an appropriate requirement, the same Z-tagged muon sample is used. The $|d_0|/\sigma_{d_0}$ distribution of prompt muons in the Z-tagged

control sample is shown in Figure 7.4. To preserve high signal efficiency, muon candidates are required to have d_0 within three standard deviations of the beam axis (i.e. $|d_0|/\sigma_{d_0} < 3$).

7.4 $W^{\pm}Z$ Selection

The $\ell^{\pm}\nu_{\ell}\ell'^{+}\ell'^{-}$ decay channel is selected from the sample of events satisfying the trigger and DQ requirements using the selected electrons and muons, plus the reconstructed $E_{\mathrm{T}}^{\mathrm{miss}}$, in five steps. First, events are required to contain a Z-boson candidate. Next, each event is required to have at least three high-p_{T} leptons plus large $E_{\mathrm{T}}^{\mathrm{miss}}$. Then, each event is required to have a W-boson candidate. Finally, each event is required to have been triggered by a decay product of the $W^{\pm}Z$-system.

7.4.1 Z Selection

Z-boson candidates are reconstructed by forming opposite-sign same flavor (OSSF) lepton pairs from the selected electrons and muons. In events containing more than one OSSF pair, the Z-boson candidate is formed from the pair with invariant mass closest to the Z-boson mass.

The di-lepton invariant mass distribution after all other event selection is shown in Figure 7.5. The backgrounds are estimated using simulation as described in Chapter 8. Events are selected only if the invariant mass of the Z-boson candidate is within 10 GeV of the Z mass. This preserves high detection efficiency while rejecting most of the background.

7.4.2 Tri-Lepton+$E_{\mathrm{T}}^{\mathrm{miss}}$ Selection

In addition to the Z-boson candidate, another lepton is needed to reconstruct a $W^{\pm}Z$ candidate. The p_{T} distribution of the third lepton is shown in Figure 7.6. To reject the background from non-prompt leptons and mis-identified hadrons, the lepton is required to have $p_{\mathrm{T}} > 20$ GeV.

The $E_{\mathrm{T}}^{\mathrm{miss}}$ distribution in tri-lepton events with this p_{T} requirement is shown in Figure 7.7. Given the high mass of the W-boson, the neutrinos produced in decays thereof tend to be relatively energetic, resulting in large $E_{\mathrm{T}}^{\mathrm{miss}}$. In contrast, the $E_{\mathrm{T}}^{\mathrm{miss}}$ in the $Z+$jets, $Z\gamma$, and ZZ backgrounds is typically produced by mis-measurement of the energies and/or momenta of various objects used in the $E_{\mathrm{T}}^{\mathrm{miss}}$ reconstruction, typically amounting to $\sim 10-20$ GeV. Therefore, to reject the bulk of this background, events are required to have $E_{\mathrm{T}}^{\mathrm{miss}} > 25$ GeV.

7.4.3 W Selection

The W-boson candidate is identified by reconstructing its transverse mass (m_{T}). The mass is calculated from the $E_{\mathrm{T}}^{\mathrm{miss}}$, which is assumed to be produced entirely by a neutrino, and

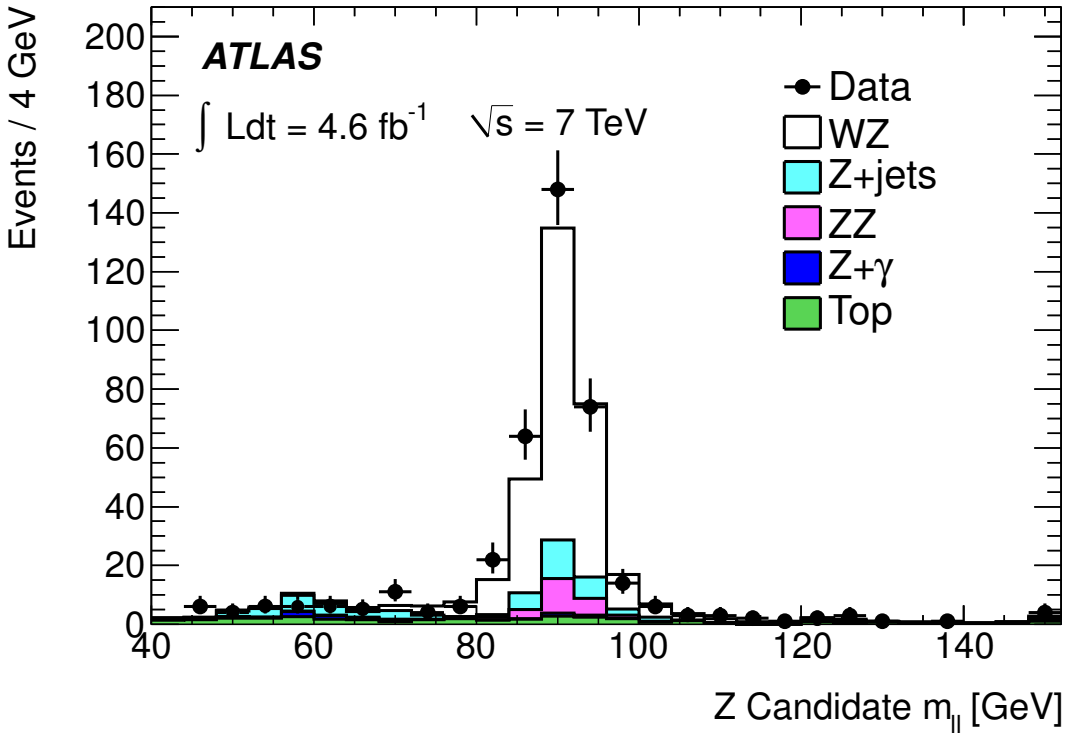

Figure 7.5: The di-lepton invariant mass distribution, after all event selection has been imposed except the Z-mass requirement. The signal is shown as an open histogram on top of the multi-colored stack of background histograms; the data points are shown with error bars representing the 68% confidence interval based on Poisson statistics.

the transverse momentum of the highest-p_{T} lepton in the event not associated with the Z-boson candidate as:

$$m_{\mathrm{T}} = \sqrt{\left(E_{\mathrm{T}}^{\ell} + E_{\mathrm{T}}^{\mathrm{miss}}\right)^2 - \left(\mathbf{p}_{\mathrm{T}}^{\ell} + \mathbf{E}_{\mathrm{T}}^{\mathrm{miss}}\right)^2}, \tag{7.2}$$

where $\mathbf{E}_{\mathrm{T}}^{\mathrm{miss}}$ is the 3-vector: $\left(E_{\mathrm{T},x}^{\mathrm{miss}}, E_{\mathrm{T},y}^{\mathrm{miss}}, 0\right)$. The m_{T} distribution is shown in Figure 7.8. To reject the low-m_{T}, off-shell W^* contribution from heavy-flavor hadron decays, W-boson candidates are required to have $m_{\mathrm{T}} > 20$ GeV.

7.4.4 Trigger Matching

To ensure the validity of the trigger simulation, events are required to have been triggered by one of the three leptons reconstructed as having been produced in the decays of the W- and Z-bosons. This is accomplished by requiring that at least one trigger object that satisfied one of the EF algorithms must have been reconstructed with $\Delta R < 0.15$ (0.10)

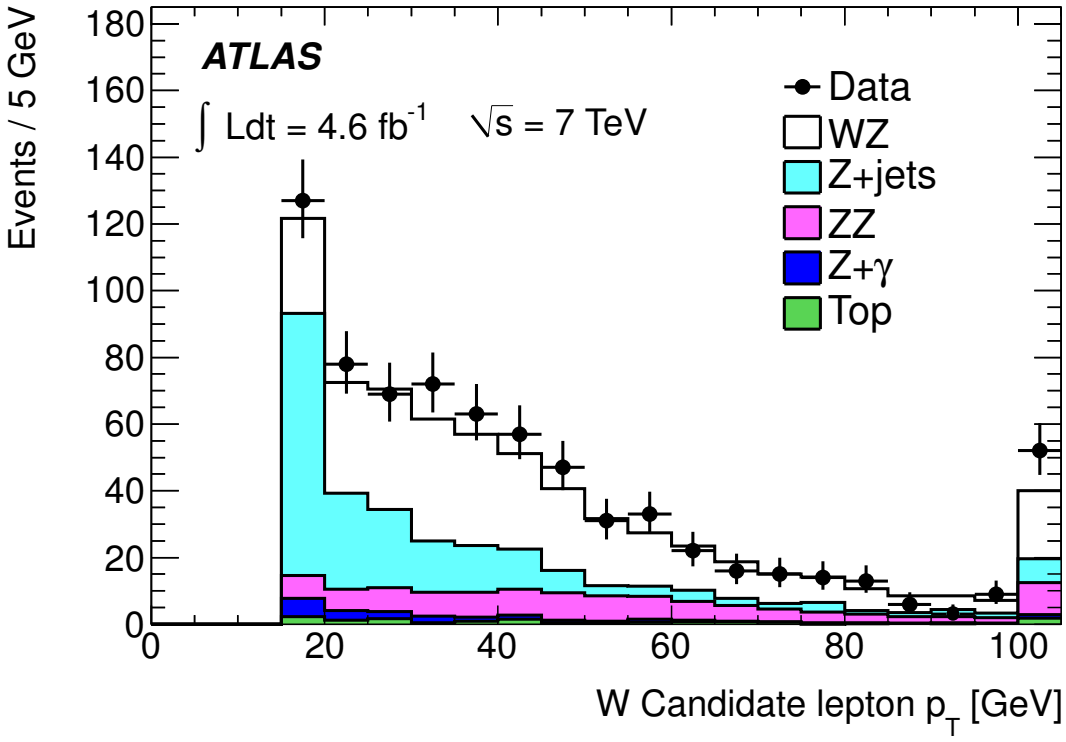

Figure 7.6: p_{T} distribution of the bachelor lepton in tri-lepton events. The signal is shown as an open histogram on top of the multi-colored stack of background histograms; the data points are shown with error bars representing the 68% confidence interval based on Poisson statistics.

relative to one of the selected electrons (muons) reconstructed offline as coming from a vector boson decay. This test is only imposed on a lepton if it is in the well-understood efficiency region, which is $p_{\mathrm{T}} > 25$ (20) GeV for electrons (muons).

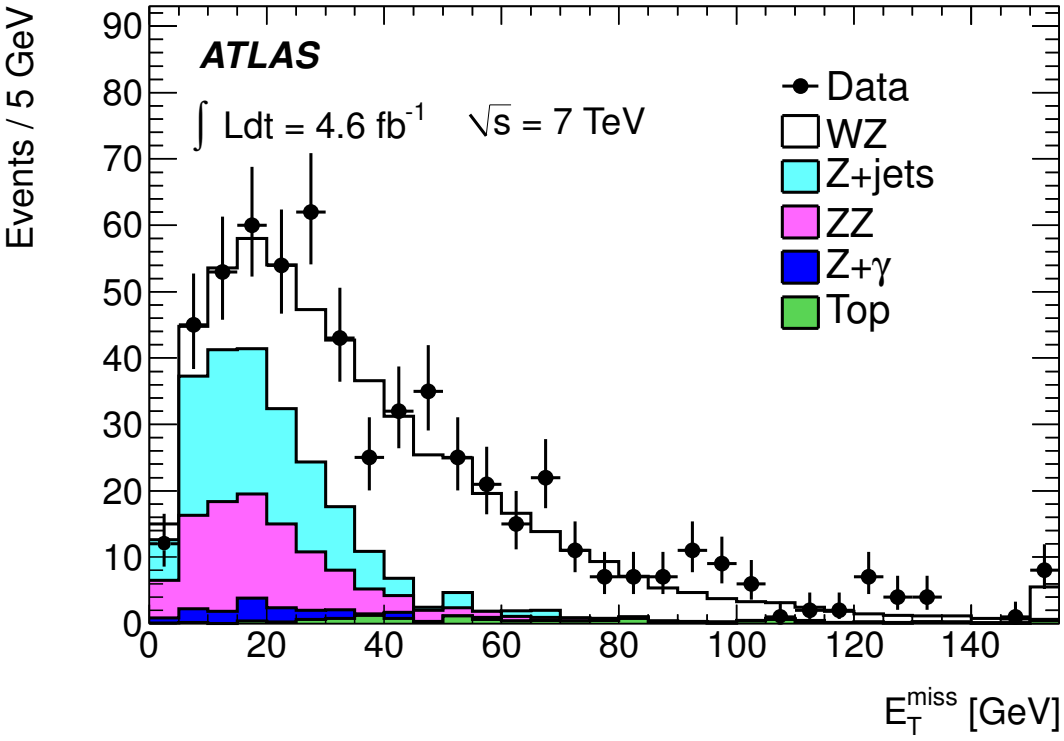

Figure 7.7: $E_{\mathrm{T}}^{\mathrm{miss}}$ distribution in tri-lepton events satisfying the Z-mass and bachelor lepton-p_{T} requirements. The signal is shown as an open histogram on top of the multi-colored stack of background histograms; the data points are shown with error bars representing the 68% confidence interval based on Poisson statistics.

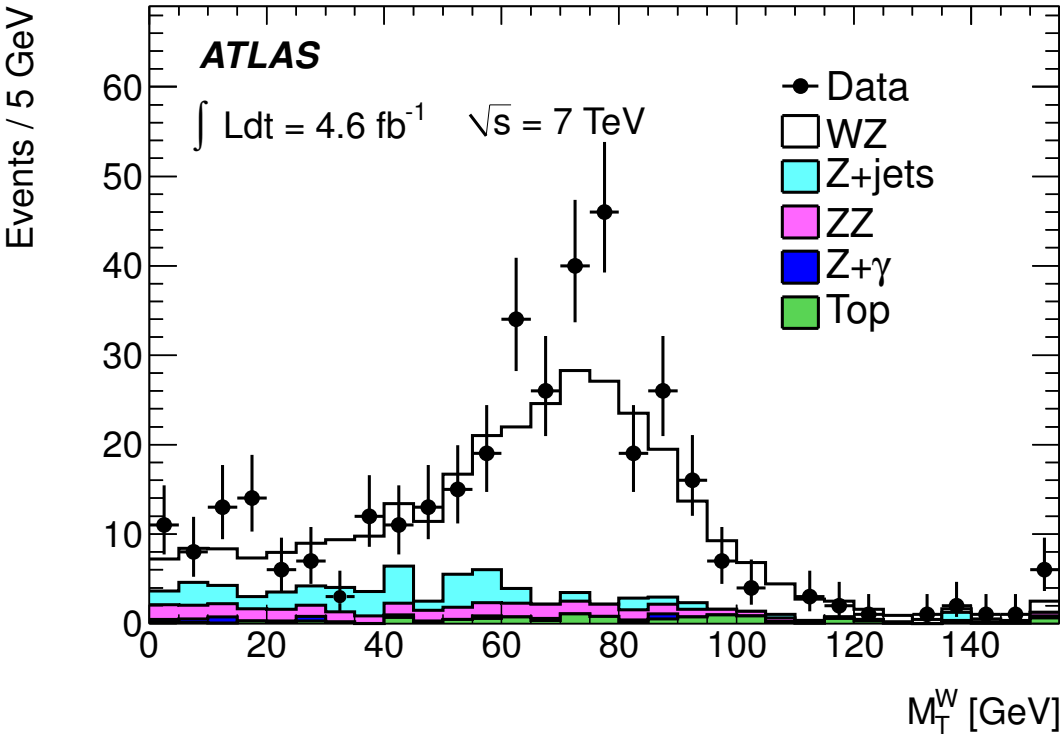

Figure 7.8: Transverse mass distribution of W-boson candidates. The signal is shown as an open histogram on top of the multi-colored stack of background histograms; the data points are shown with error bars representing the 68% confidence interval based on Poisson statistics.

Chapter 8
Background Estimations

The background contribution to the tri-lepton+$E_{\mathrm{T}}^{\mathrm{miss}}$ signature can be divided into three categories: events containing at least three prompt leptons from vector boson decays produced in processes other than $W^{\pm}Z$, events containing some combination of prompt leptons and converted photons reconstructed as electrons, and events containing at least one mis-identified hadron or non-prompt lepton produced in a hadronic decay in addition to some number of prompt leptons. The former two categories of backgrounds are estimated using only MC simulation, while the latter category of backgrounds is estimated using data.

8.1 Monte Carlo Background Estimation

The background processes estimated using simulation include: ZZ, $t\bar{t}V$, and $Z\gamma$.

8.1.1 ZZ Background

The ZZ contribution to the tri-lepton+$E_{\mathrm{T}}^{\mathrm{miss}}$ signature is from events in which the ZZ system decays via the four-lepton channel, with one lepton either escaping detection entirely (e.g. outside of the detector acceptance) or failing to satisfy the strict lepton selection outlined in Sections 7.2 and 7.3 (e.g. being coincident with activity from the underlying event or a pile-up event and thereby failing the isolation requirement), in conjunction with a substantial quantity of $E_{\mathrm{T}}^{\mathrm{miss}}$ produced by mis-measurement or non-prompt neutrinos from hadron decays. The SM expectation for such events can be estimated by applying the event selection outlined in Chapter 7 to the ZZ MC sample listed in Table 6.1. The expected event yield from this process is listed in Table 10.1.

8.1.2 $t\bar{t}V$

The $t\bar{t}V$ contribution to the tri-lepton+$E_{\mathrm{T}}^{\mathrm{miss}}$ signature is primarily from $t\bar{t}Z$ events. The reaction of interest is $t\bar{t}Z \rightarrow W^{+}W^{-}b\bar{b}Z$, where one W-boson decays leptonically. There is also a contribution from $t\bar{t}W^{\pm}$ events, which decay to $W^{+}W^{-}b\bar{b}W^{\pm}$. When all three

W-bosons decay leptonically, they produce three prompt leptons plus large $E_{\mathrm{T}}^{\mathrm{miss}}$ from the three high-p_{T} neutrinos. As in the case of ZZ, these backgrounds are modeled by applying the full event selection to the MC samples listed in Table 6.1, and the resulting estimates of the expected event yields are listed in Table 10.1.

8.1.3 $Z\gamma$

The $Z\gamma$ contribution to the tri-lepton+$E_{\mathrm{T}}^{\mathrm{miss}}$ signature is from events where the Z-boson decays leptonically and the photon converts in the first layers of the ID, but the conversion is not properly identified. As in the case of ZZ, the $E_{\mathrm{T}}^{\mathrm{miss}}$ in $Z\gamma$ events is from mis-measurement or non-prompt neutrinos from hadron decays. As with the other backgrounds estimated from simulation, the expected event yield from $Z\gamma$ is estimated using the MC sample listed in Table 6.1, and the result is listed in Table 10.1.

8.2 Data-Driven Background Estimation

Since the hadronic decay processes and hadron-calorimeter interactions that produce non-prompt leptons and hadron mis-identification are not as well understood as conversions or the interactions of prompt leptons with the detector, the simulation of such phenomena is not completely reliable. As such, data-driven methods are used to estimate the contributions to the signal region from mis-identified hadrons and non-prompt leptons. Such contributions are expected to be dominated by two physics processes: $Z+\text{jets}$ and $t\bar{t}$. Each is estimated separately using a dedicated method.

8.2.1 $Z+\text{jets}$: Fake-Factor Method

The contribution of $Z+\text{jets}$ to the tri-lepton+$E_{\mathrm{T}}^{\mathrm{miss}}$ signature is mostly due to a light-flavor hadron in a jet mis-identified as an electron or a lepton from the decay of a heavy-flavor hadron in such a jet. The $E_{\mathrm{T}}^{\mathrm{miss}}$ in such events can be produced by mis-measurement or non-prompt neutrinos from hadron decays, as in the cases of ZZ and $Z\gamma$. To estimate the expected event yield in the signal region due to this process, the "fake-factor" method is used, as detailed below.

Lepton-Like Jets

In order to use the "fake-factor" method to estimate the $Z+\text{jets}$ contribution, the jets are first classified by whether they are lepton-like. A lepton-like jet is defined as a jet containing either a light-flavor hadron that deposits significant energy in the EM calorimeter to satisfy all electron selection criteria aside from loose++ or isolation, or a muon produced in the decay of a hadron that satisfies all muon selection criteria aside from ID track isolation.

Selecting leptons that fail the electron loose++ and isolation requirements and the muon isolation requirement allows for the construction of a control sample of reconstructed objects that were presumably not actually prompt leptons. Although they fail the lepton selection requirements, these lepton-like jets could conceivably fluctuate from the failing state to the passing state, and are therefore useful for extrapolating the properties of those non-prompt leptons and mis-identified hadrons that do pass the requirements and thereby contaminate the signal region.

Fake-Factor Measurement

The ratio of leptons to lepton-like jets is measured in a control sample of events containing a Z-boson, an extra object, and low $E_{\mathrm{T}}^{\mathrm{miss}}$ (< 25 GeV). The contribution from $t\bar{t}$ production is estimated as per Section 8.2.2 and all other background contributions (i.e. $W^{\pm}Z$ and ZZ) are estimated from simulation. After subtracting these contributions, the "fake-factor" is measured as the pass:fail ratio of the selection criteria that distinguish lepton-like jets from lepton candidates:

$$f\left(\ell, E_{\mathrm{T}}^{\mathrm{miss}}\right) = \frac{N\left(Z+\ell, E_{\mathrm{T}}^{\mathrm{miss}}\right) - N_{\mathrm{B}}\left(Z+\ell, E_{\mathrm{T}}^{\mathrm{miss}}\right)}{N\left(Z+\ell_{\mathrm{jet}}, E_{\mathrm{T}}^{\mathrm{miss}}\right) - N_{\mathrm{B}}\left(Z+\ell_{\mathrm{jet}}, E_{\mathrm{T}}^{\mathrm{miss}}\right)}, \tag{8.1}$$

where N_{B} is the aforementioned background correction term and ℓ_{jet} denotes a lepton-like jet. The "fake-factor" is measured in bins of Z-boson p_{T}, as discussed in Section 11.1.

$E_{\mathrm{T}}^{\mathrm{miss}}$ Scaling

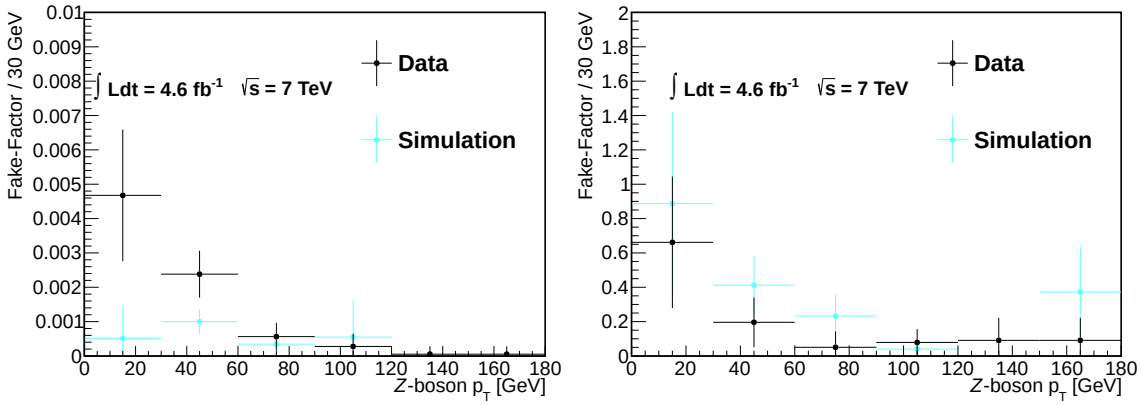

(a) (b)

Figure 8.1: The measured and simulated "fake-factors" for (a) electrons and (b) muons.

The assumption underlying the "fake-factor" method is that, since the $E_{\mathrm{T}}^{\mathrm{miss}}$ in $Z+$jets events is produced by mis-measurement and any non-prompt neutrinos in the jets, the $E_{\mathrm{T}}^{\mathrm{miss}}$ in $Z+$jets events is largely independent of the precise details (especially the flavor and the fraction of energy deposited in the EM calorimeter) of the hadrons within those jets. Therefore, the "fake-factor" can be measured in the low-$E_{\mathrm{T}}^{\mathrm{miss}}$ control region and extrapolated to the adjacent high-$E_{\mathrm{T}}^{\mathrm{miss}}$ (> 25 GeV) region. Calculating the "fake-factor" in the $Z+$jets MC sample listed in Table 6.1, in both the low-$E_{\mathrm{T}}^{\mathrm{miss}}$ and high-$E_{\mathrm{T}}^{\mathrm{miss}}$ regions, allows for an extrapolation from the low-$E_{\mathrm{T}}^{\mathrm{miss}}$ control region to the high-$E_{\mathrm{T}}^{\mathrm{miss}}$ control region, as:

$$f^{\mathrm{Data}}\left(\ell, E_{\mathrm{T}}^{\mathrm{miss}} > 25 \text{ GeV}\right) = f^{\mathrm{Data}}\left(\ell, E_{\mathrm{T}}^{\mathrm{miss}} < 25 \text{ GeV}\right) \times \frac{f^{\mathrm{MC}}\left(\ell, E_{\mathrm{T}}^{\mathrm{miss}} > 25 \text{ GeV}\right)}{f^{\mathrm{MC}}\left(\ell, E_{\mathrm{T}}^{\mathrm{miss}} < 25 \text{ GeV}\right)}, \quad (8.2)$$

where $f^{\mathrm{Data}}\left(\ell, E_{\mathrm{T}}^{\mathrm{miss}} > 25 \text{ GeV}\right)$ is the extrapolated "fake-factor" applicable in the high-$E_{\mathrm{T}}^{\mathrm{miss}}$ region. The "fake-factor" simulated in both the low- and high-$E_{\mathrm{T}}^{\mathrm{miss}}$ regions are consistent with each other, so the central value of the $E_{\mathrm{T}}^{\mathrm{miss}}$ extrapolation factor in Equation 8.2 is set to unity. The measured and simulated electron and muon "fake-factors" are shown in Figure 8.1. As expected, the simulation is not entirely accurate, especially for electrons at low-p_{T}.

Fake-Factor Application/Background Estimation

Using the extrapolated "fake-factor", the contribution to the signal region from $Z+$ jets events can then be estimated using a control region defined as the set of events which pass the full event selection except that there are two prompt leptons and one lepton-like jet instead of three prompt leptons. This estimation is accomplished by scaling each event with a lepton-like jet by the "fake-factor". However, $\sim$15% of the sample of events with one lepton-like jet are actually events with one prompt lepton, one lepton-like jet, and one lepton-like jet that has fluctuated from the failing state to the passing state. This contamination is estimated by selecting events containing one prompt lepton plus two lepton-like jets and scaling each event by the product of the "fake-factors" for the two lepton-like jets. The background contribution to the $Z+$ jets control regions is subtracted before the "fake-factor" is applied. Thus, the expected contribution to the signal region from $Z+$jets events is calculated as:

$$
\begin{aligned}
N_{\text{Bkg}} \quad = \quad & \left(N\left(\ell^1\ell^2\ell^3_{\text{jet}}, E_{\text{T}}^{\text{miss}} > 25\text{ GeV}\right) - N_{\text{B}}\left(\ell^1\ell^2\ell^3_{\text{jet}}, E_{\text{T}}^{\text{miss}} > 25\text{ GeV}\right)\right) \\
& \times f^{\text{Data}}\left(\ell^3, E_{\text{T}}^{\text{miss}} > 25\text{ GeV}\right) \\
& - \left(N\left(\ell^1\ell^2_{\text{jet}}\ell^3_{\text{jet}}, E_{\text{T}}^{\text{miss}} > 25\text{ GeV}\right) - N_{\text{B}}\left(\ell^1\ell^2_{\text{jet}}\ell^3_{\text{jet}}, E_{\text{T}}^{\text{miss}} > 25\text{ GeV}\right)\right) \\
& \times f^{\text{Data}}\left(\ell^2, E_{\text{T}}^{\text{miss}} > 25\text{ GeV}\right) \times f^{\text{Data}}\left(\ell^3, E_{\text{T}}^{\text{miss}} > 25\text{ GeV}\right).
\end{aligned} \tag{8.3}
$$

As with the other sources of background, the expected event yield from $Z+\text{jets}$ is given in Table 10.1.

8.2.2 $t\bar{t}$: Scale-Factor Method

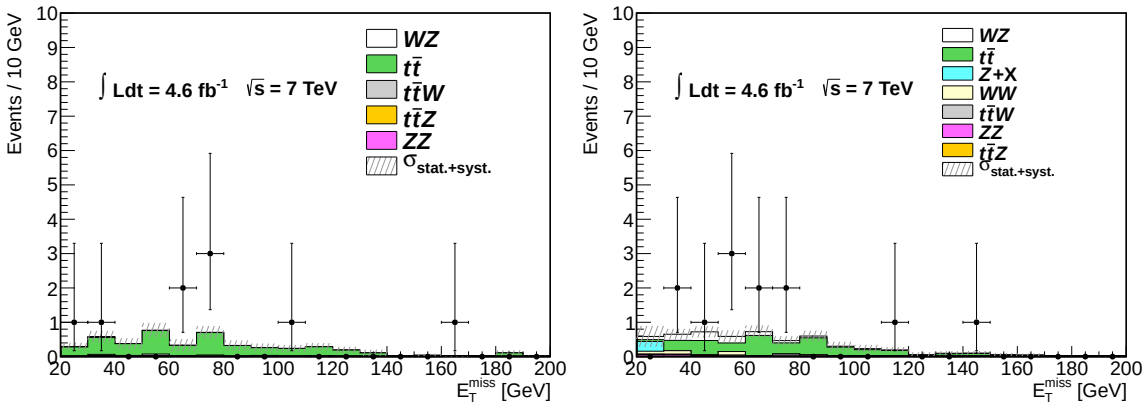

(a) (b)

Figure 8.2: The simulated and measured $E_{\text{T}}^{\text{miss}}$ distribution in the same-sign lepton pair Z-boson candidate control region in the (a) $e\nu\mu\mu$ and (b) $\mu\nu ee$ channels.

In $t\bar{t}$ events, the top-quarks mainly decay as: $t\bar{t} \rightarrow W^+W^-b\bar{b}$. As a result, the $t\bar{t}$ contribution to the tri-lepton+$E_{\text{T}}^{\text{miss}}$ signature is due to non-prompt leptons from the decays of b-hadrons in conjunction with two prompt leptons from leptonic decays of the W-bosons. Since there is some uncertainty as to the reliability of the simulation of these non-prompt leptons, the estimated $t\bar{t}$ background yield from simulation is normalized to the data in a $t\bar{t}$-enriched control region, defined as the region containing three lepton candidates that pass the prompt lepton selection and that, in conjunction with large-$E_{\text{T}}^{\text{miss}}$ produced by the high-p_{T} neutrinos from the W-boson decays, satisfy the full event selection, except that the Z-boson candidate is reconstructed using a same-sign, same-flavor lepton pair (viz. e^+e^+, e^-e^-, $\mu^+\mu^+$, or $\mu^-\mu^-$). The same-flavor channels (viz. $e\nu ee$ and $\mu\nu\mu\mu$) are excluded to

remove any combinatoric effects (i.e. wherein the leptons from the W- and Z-boson decays could be confused). The expected and observed yields in the two different-flavor channels (viz. $e\nu\mu\mu$ and $\mu\nu ee$) are shown in Figure 8.2. To enhance the purity of the sample used to calculate the normalization scale-factor (SF), only the subset with 60 GeV $< E_{\mathrm{T}}^{\mathrm{miss}} <$ 200 GeV is considered in the $\mu^{\pm}\nu_{\mu}e^{+}e^{-}$ channel. The observed yields are consistently above the expectation from simulation, resulting in an overall SF of 2.2. This SF is then applied to the simulated event yield determined by applying the full event selection to the $t\bar{t}$ MC sample listed in Table 6.1 to get the data-driven expected event yield. As with the other sources of background, this expected yield is given in Table 10.1.

Chapter 9
Systematic Uncertainties

The systematic uncertainties in the event yield can be divided into two categories: uncertainties in the simulation and uncertainties in backgrounds estimated using the data. All uncertainties are calculated both for each lepton flavor channel and as a function of Z-boson p_{T}.

9.1 Simulation

Two types of simulation uncertainties are estimated: theoretical uncertainties and experimental uncertainties. Theoretical uncertainties arise from the choice of generator used for the ME calculation, the PDF set used, and the choice of theoretical scale parameters. Experimental uncertainties arise from potential imperfect modeling of pile-up, detection efficiencies, energy/momentum scales and resolutions, and from the uncertainty in the integrated luminosity. The uncertainties in various aspects of the simulation are calculated using the signal sample generated with SM couplings. The same fractional uncertainties are assumed to also apply to the samples generated with non-SM couplings and, in the case of experimental uncertainties, to the background process simulations as well. The theoretical uncertainties in the background simulations are determined separately. The fractional uncertainties in simulated signal yield from each of the sources is given for each lepton flavor channel in Table 9.1 and as a function of Z-boson p_{T} in Table 9.2.

9.1.1 Generator

The uncertainty in the generator used in the ME calculation is evaluated as the difference between the results simulated with MC@NLO and those simulated using an alternative generator (PowhegBox [39]).

Source	$e^{\pm}\nu_e e^+e^-$	$\mu^{\pm}\nu_\mu e^+e^-$	$e^{\pm}\nu_e \mu^+\mu^-$	$\mu^{\pm}\nu_\mu \mu^+\mu^-$
μ reconstruction efficiency	-	0.27	0.53	0.80
μ p_{T} scale & resolution	-	0.04	0.05	0.06
μ isolation & impact param.	-	0.20	0.43	0.62
e reconstruction efficiency	2.5	1.7	0.8	-
e identification efficiency	3.5	2.3	1.2	-
e isolation & impact param.	1.5	1.1	0.4	-
e energy scale	0.5	0.3	0.3	-
e energy resolution	0.1	0.1	0.0	-
$E_{\mathrm{T}}^{\mathrm{miss}}$ topocluster energy scale	0.40	0.17	0.57	0.18
$E_{\mathrm{T}}^{\mathrm{miss}}$ jet energy scale	0.11	0.08	0.10	0.08
$E_{\mathrm{T}}^{\mathrm{miss}}$ jet energy resolution	0.28	0.30	0.39	0.25
$E_{\mathrm{T}}^{\mathrm{miss}}$ pile-up	0.32	0.11	0.32	0.13
Muon trigger	-	0.07	0.15	0.29
Electron trigger	<0.05	<0.05	<0.05	-
Event generator	0.4	0.4	0.4	0.4
PDF	1.2	1.2	1.2	1.2
QCD scale	0.4	0.4	0.4	0.4
Luminosity	1.8	1.8	1.8	1.8

Table 9.1: Fractional uncertainties (%) on the simulated signal yield from various sources in each lepton flavor channel.

9.1.2 PDF

The uncertainty in the PDF set used in the simulation is determined using the 52 error eigenvectors of the CT10 set, and then adding in quadrature the difference between the expected yield calculated using the CT10 and MSTW2008 [40] PDF sets.

9.1.3 Scale

The signal expectation is calculated with QCD factorization and renormalization scales both fixed at the Z-boson mass. To evaluate the uncertainty introduced by this choice, the signal expectation is recalculated varying the scales up and down by a factor of two. The variation in the expectation is used as the uncertainty.

9.1.4 Pile-up

There are two potential issues with the pile-up simulation: the modeling of the number of pile-up interactions and the calorimeter response to each one.

Source \ p_{T} (GeV)	0-30	30-60	60-90	90-120	120-150	150-180	180-2000
μ reconstruction efficiency	0.55	0.56	0.57	0.58	0.59	0.61	0.63
μ p_{T} scale & resolution	0.07	0.03	0.07	0.18	0.35	0.15	0.25
μ isolation & impact param.	0.32	0.43	0.49	0.53	0.55	0.57	0.55
e reconstruction efficiency	0.97	0.97	1.19	1.03	1.06	0.10	1.13
e identification efficiency	1.35	1.44	0.94	1.44	1.37	0.55	1.30
e isolation & impact param.	0.41	0.56	0.79	0.70	0.70	0.03	0.73
e energy scale	-0.16	0.16	0.10	0.38	0.40	-0.43	1.10
e energy resolution	0.05	0.02	-0.28	-0.07	0.09	0.51	-0.14
$E_{\mathrm{T}}^{\mathrm{miss}}$ cluster energy scale	-0.00	0.20	0.41	0.47	0.19	0.06	-0.12
$E_{\mathrm{T}}^{\mathrm{miss}}$ jet energy scale	-0.07	-0.09	-0.23	0.04	-0.16	0.35	0.04
$E_{\mathrm{T}}^{\mathrm{miss}}$ jet energy resolution	-0.01	0.01	0.27	0.36	-0.07	0.05	0.61
$E_{\mathrm{T}}^{\mathrm{miss}}$ pile-up	0.04	0.10	0.35	0.36	0.08	0.04	-0.21
Muon Trigger	0.14	0.16	0.16	0.16	0.15	0.14	0.14
Electron Trigger	0.02	0.03	0.03	0.03	0.02	0.02	0.02
Event generator	-0.58	-2.97	3.90	1.11	1.10	4.28	-1.45
PDF	4.28	4.19	4.09	4.00	4.16	4.02	4.24
QCD Scale	2.60	2.60	4.80	8.70	6.70	7.30	8.00
Luminosity	1.8	1.8	1.8	1.8	1.8	1.8	1.8

Table 9.2: Fractional uncertainties (%) on the simulated signal yield from various sources as a function of Z-boson p_{T}. The relative sign in different p_{T} ranges denotes the relative phase of the results from each variation.

Pile-up Reweighting

Averaging over a bunch train, the number of pile-up interactions per bunch crossing, denoted $\langle\mu\rangle$, is simulated using four sets of hypothetical conditions. For each set of conditions expected during a particular set of LHC fills, the simulated $\langle\mu\rangle$ distribution are reweighted to reflect the observed $\langle\mu\rangle$ distributions during that set. This process does not introduce additional uncertainty beyond the luminosity uncertainty described in Section 9.1.7, however it does increase the statistical uncertainty in events with $\langle\mu\rangle$ values more prevalent in the data than was simulated.

Pile-up Energy Response

The simulated calorimeter response to pile-up events is evaluated by studying the scalar sum of E_{T} as a function of the number of pile-up events. A 6.6% uncertainty is assigned to the topocluster term in Equation 5.3. The $E_{\mathrm{T}}^{\mathrm{miss}}$ is recalculated in each event varying the term $\pm1\sigma$, and the resulting variation in the expected signal yield is used as the uncertainty.

9.1.5 Efficiencies

The GEANT4 simulation is conducted on all MC samples using a single set of detector conditions, with a hypothetical detector response. This can systematically bias the simulated efficiency for detecting a particle. To correct for this, the simulated pass probability of each set of selection criteria is corrected using a SF, defined as the pass probability ratio of data to simulation, derived using W/Z T&P. The SF is applied to the weight of each event, so that the resulting aggregate distribution of passing events reflects the probability measured in data. Since the trigger requirement is that the logical OR of the electron and muon triggers be satisfied by one of the three leptons, the individual lepton trigger efficiency measured using Z T&P is taken into account as an event-level trigger SF. The central value of the expected event yield is calculated by applying the central values of all SFs. The uncertainty in each SF is then translated into an uncertainty in the simulated event yield by varying each SF by $\pm1\sigma$. The SFs used in this analysis are:

- electron reconstruction
- electron identification
- electron isolation & impact parameter
- muon reconstruction
- muon isolation & impact parameter
- trigger

The total effect of these SF is shown on the penultimate line of Table 7.1.

Electron Reconstruction

The efficiency of the electron reconstruction algorithm described in Section 5.1 is measured using W and Z T&P as a function of p_{T} and η.

Electron Identification

The combined efficiency of the standard electron quality requirements and sets of identification criteria described in Section 7.2.1 is measured using W and Z T&P as a function of p_{T} and η.

Electron Isolation & Impact Parameter

The combined efficiency of the set of electron isolation amd impact parameter requirements described in Section 7.2.2 is measured using Z T&P as a function of p_{T} and η.

Muon Reconstruction

The efficiency of the muon reconstruction algorithms described in Section 5.2 is measured using Z T&P as a function of p_{T} and η.

Muon Isolation & Impact Parameter

The efficiency of the set of muon isolation and impact parameter requirements described in Section 7.3.2 is measured using Z T&P as a function of p_{T} and η.

Trigger

Since different triggers were used over the course of the data-taking (Table 3.1), each simulated event is randomly assigned to a fill corresponding to the simulated pile-up conditions, based on the relative luminosity fractions of different fills. The triggers required in each event are then the triggers required during the corresponding data-taking. The probabilities of reconstructed electrons or muons satisfying each of the triggers used in this analysis are calculated, and single-lepton SFs are derived, using several Z T&P studies, as a function of p_{T} and η. The single-lepton SFs for each of the three $W^{\pm}Z$ leptons in an event are

translated into an event-level trigger SF using the formula:

$$\begin{aligned} \mathrm{SF} &= \frac{\varepsilon_{\mathrm{Data}}}{\varepsilon_{\mathrm{MC}}} \\ &= \frac{1-(1-\varepsilon_{\mathrm{Data}})}{1-(1-\varepsilon_{\mathrm{MC}})} \\ &= \frac{1-\left(1-\varepsilon^{1}_{\mathrm{Data}}\right)\times\left(1-\varepsilon^{2}_{\mathrm{Data}}\right)\times\left(1-\varepsilon^{3}_{\mathrm{Data}}\right)}{1-\left(1-\varepsilon^{1}_{\mathrm{MC}}\right)\times\left(1-\varepsilon^{2}_{\mathrm{MC}}\right)\times\left(1-\varepsilon^{3}_{\mathrm{MC}}\right)}. \end{aligned} \tag{9.1}$$

where ε is the total event-level trigger efficiency and ε^{i} is the trigger efficiency of the i^{th} lepton in the event. Given that the single-lepton trigger SF is defined as:

$$\mathrm{SF^{i}} = \frac{\varepsilon^{i}_{\mathrm{Data}}}{\varepsilon^{i}_{\mathrm{MC}}}, \tag{9.2}$$

the total event-level SF is thus:

$$\mathrm{SF} = \frac{1-\left(1-\varepsilon^{1}_{\mathrm{MC}}\times\mathrm{SF}^{1}\right)\times\left(1-\varepsilon^{2}_{\mathrm{MC}}\times\mathrm{SF}^{2}\right)\times\left(1-\varepsilon^{3}_{\mathrm{MC}}\times\mathrm{SF}^{3}\right)}{1-\left(1-\varepsilon^{1}_{\mathrm{MC}}\right)\times\left(1-\varepsilon^{2}_{\mathrm{MC}}\right)\times\left(1-\varepsilon^{3}_{\mathrm{MC}}\right)}. \tag{9.3}$$

The variations in the calculated event-level scale factor used to determine the electron and muon trigger uncertainties in the expected event yield are determined by varying the electron and muon single-lepton SF separately.

9.1.6 Scale & Resolution

Energy/momentum scales and resolutions (i.e. Gaussian widths) affect both the probability that a lepton will pass the p_{T} requirement to be selected and the energy/momentum/mass distributions of composit objects such as $E_{\mathrm{T}}^{\mathrm{miss}}$ and vector boson candidates. In calculating the central value of the expected event yield, the assumed lepton resolutions used for the GEANT4 simulation are smeared. Since the convolution of two Gaussian distributions is a Gaussian distribution whose width is the quadratic sum of the widths of the input distributions, each energy/momentum is scaled by a factor randomly taken from a Gaussian whose width (σ_{Δ}), when combined in quadrature with the width assumed in the simulation (σ_{MC}), reproduces the width observed in data (σ_{Data}), as:

$$\sigma^{2}_{\mathrm{Data}} = \sigma^{2}_{\mathrm{MC}} + \sigma^{2}_{\Delta}. \tag{9.4}$$

The uncertainties in the expected event yield are then determined as the variation in signal yield produced by varying each energy scale or resolution $\pm 1\sigma$. The dominant sources of scale and resolution uncertainties are those from electron energy, muon momentum, and jet energy (which dominates the $E_{\mathrm{T}}^{\mathrm{miss}}$ calculation).

Electron Energy and Muon Momentum Scale & Resolution

The electron energy and muon momentum scales used to reconstruct data and the resolutions used to smear the simulation are determined for each flavor, using separate Z T&P studies, as a function of p_{T} and η, factorizing the dependence on each. The uncertainties in the measured Z-masses used to derive the calibrations are used as the uncertainties in the scales. The widths of the resolution models used in the mass fits are used as resolutions.

Jet Energy Scale

The jet energy scale is determined as a function of p_{T}, η, ϕ, $\langle\mu\rangle$, and the number of reconstructed vertices in the event using di-jet T&P, wherein a sample of events containing two high-p_{T} jets that recoil off of each other is identified and the imbalance in the jet energies is assumed to be caused by uncertainties in the calibrations of the calorimeter cells in which the energy was deposited.

Jet Energy Resolution

The jet energy resolution is determined as a function of p_{T} and η using di-jet T&P. Although the resolution used in the simulation is used as the central value, when performing the variations in resolution to get the uncertainty, the energies of all jets in the event are smeared using the same Gaussian procedure as is used for leptons with the resolution set to be large enough to encompass the shift in central value.

Topocluster Energy Scale

A 10-13% uncertainty in the topocluster energy scale is determined by comparing the energy of topoclusters to the momenta of matching ID tracks.

9.1.7 Luminosity

The uncertainty in the measurement of integrated luminosity is due to variations over time, the uncertainty in the total visible proton-proton scattering cross section used in its calculation, and the uncertainty in the modeling of the structure of the proton bunches.

9.1.8 Theoretical Background Uncertainties

The theoretical uncertainties in the cross section of each background process are determined separately when calculating the normalizations for the background samples, per Table 6.1.

9.2 Data-Driven Techniques

Each data-driven background estimation technique has its own uncertainties, as discussed below.

9.2.1 Fake-Factor Method

The uncertainties in the "fake-factor" estimate of the $Z+$jets background come from the statistical uncertainty in the control regions to which the "fake-factor" is applied and the uncertainties in the "fake-factor". The uncertainties in the "fake-factor" are the statistical uncertainty in the low-$E_{\mathrm{T}}^{\mathrm{miss}}$ control region, the uncertainty in the background subractions from the Z-boson candidate plus one lepton and Z-boson candidate plus one lepton-like jet control regions, and the uncertainty in the extrapolation from the low-$E_{\mathrm{T}}^{\mathrm{miss}}$ region in which the "fake-factor" is calculated to the high-$E_{\mathrm{T}}^{\mathrm{miss}}$ region in which it is applied.

Background Subtraction

The uncertainty in the subtraction of background contributions to the low-$E_{\mathrm{T}}^{\mathrm{miss}}$ control region is due to normalization uncertainty in the various samples used to estimate the contributions. The statistical uncertainty in the scale-factor (per Section 9.2.2) is used as the uncertainty in the normalization of the $t\bar{t}$ sample. The uncertainty in the most recent ATLAS cross section measurement is used as the uncertainty in each of the other subtracted samples: 20% (15%) for $W^{\pm}Z$ (ZZ). Since the various parts of the subtraction are not completely uncorrelated, the uncertainty in the expected background due to the subtraction is taken to be only half of the variation in the expected $Z+$jets background yield produced by varying the entire subtraction $\pm 1\sigma$.

$E_{\mathrm{T}}^{\mathrm{miss}}$ Extrapolation

Due to limited statistics in the $Z+$jets MC sample used to calculate the $E_{\mathrm{T}}^{\mathrm{miss}}$ extrapolation factor, and since the $E_{\mathrm{T}}^{\mathrm{miss}}$ in $Z+$jets events is, in principle, not correlated with the precise details of the jets in the event, the central value of the extrapolation factor is taken to be unity and the uncertainty is the larger of the statistical uncertainty and the difference from unity. The total uncertainty is 20% (35%) for electrons (muons). The uncertainty in the expected $Z+$jets yield is the variation produced by varying the "fake-factors" $\pm 1\sigma$.

9.2.2 Scale-Factor Method

The uncertaintes in the $t\bar{t}$ estimation are the simulation uncertainties described in Section 9.1, plus the uncertainty in the normalization SF, which comes from the statistical uncertainty in the same-sign sample. The SF is estimated to be 2.2 ± 1.0.

Chapter 10
Cross Section Measurement

The event selection is applied to the recorded data, to select $W^{\pm}Z$ candidate events. Using the expected detection efficiency for the signal process and the expected background yields, this observed event yield is converted into a measured $W^{\pm}Z$ production cross section.

10.1 Candidate Events

In 4.64 fb^{-1} of data, 317 candidate events are observed that satisfy the selection described in Chapter 7 [41]. The candidates in the four tri-lepton flavor channels, as well as the expected yields of signal and background events from the various sources, estimated per Chapter 8, is given in Table 10.1. There are 206 $W^{+}Z$ and 111 $W^{-}Z$ candidates, which is consistent with the expectations of 186 ± 11 and 110 ± 6. The p_{T} distribution of Z-bosons in $W^{\pm}Z$ candidates, together with the signal and background expectations, are shown in Figure 10.1.

Channel	$e^{\pm}\nu_e e^{+}e^{-}$	$\mu^{\pm}\nu_\mu e^{+}e^{-}$	$e^{\pm}\nu_e \mu^{+}\mu^{-}$	$\mu^{\pm}\nu_\mu \mu^{+}\mu^{-}$	$\ell^{\pm}\nu_\ell \ell'^{+}\ell'^{-}$
Observed	56	75	78	108	317
Signal	38.9±1.1±7.8	54.0±1.1±7.8	56.6±1.1±7.8	81.7±1.1±7.8	231.2±1.1±7.8
Background	14.5±5.5±8.2	11.5±5.5±8.2	21.0±5.5±8.2	21.0±5.5±8.2	68.1±5.5±8.2
Z + jets	8.8±5.3±7.5	3.7±5.3±7.5	10.2±5.3±7.5	9.1±5.3±7.5	31.9±5.3±7.5
ZZ	3.2±0.2±0.7	4.9±0.2±0.7	5.0±0.2±0.7	7.9±0.2±0.7	21.0±0.2±0.7
Top	1.1±0.9±3.4	2.9±0.9±3.4	3.5±0.9±3.4	4.0±0.9±3.4	11.5±0.9±3.4
$Z\gamma$	1.4±1.1±0.1	0.0±1.1±0.1	2.3±1.1±0.1	0.0±1.1±0.1	3.7±1.1±0.1

Table 10.1: Observed and expected event yields in the signal region for $W^{\pm}Z$ and various background processes. The top background includes both $t\bar{t}$ and $t\bar{t}V$. For the expectations, the first uncertainty is statistical, the second systematic, excluding the uncertainty in luminosity which contributes an additional 1.8%.

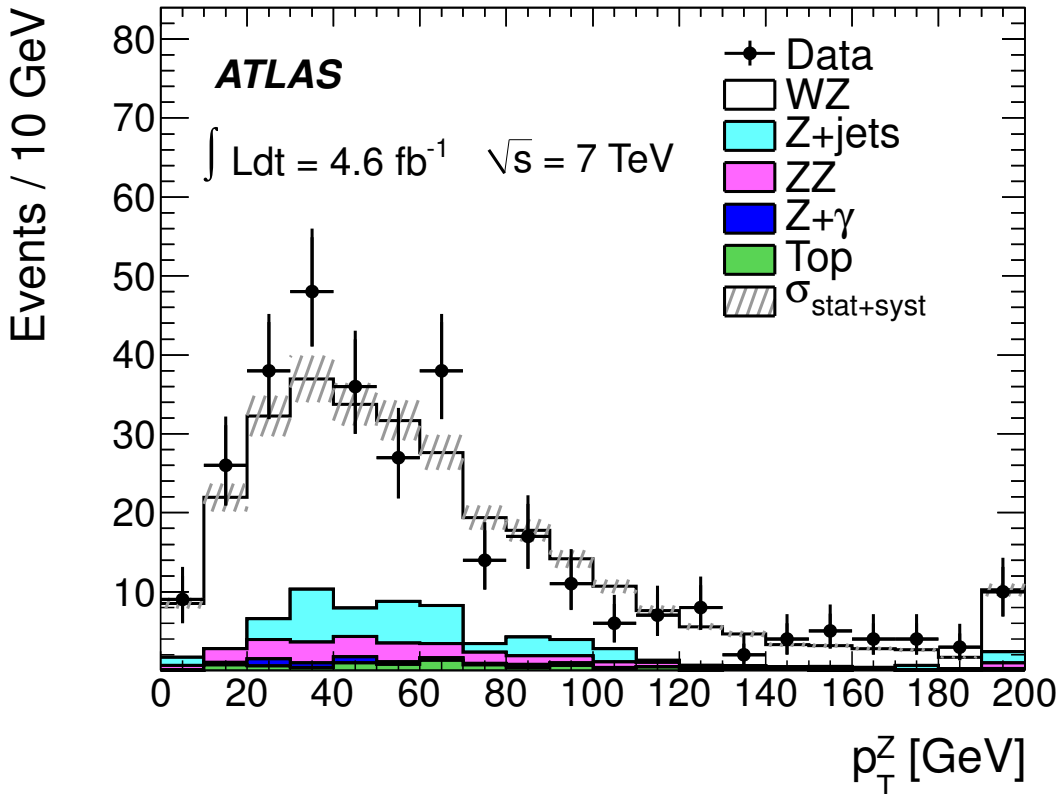

Figure 10.1: p_{T} distribution of Z-bosons in the $W^{\pm}Z$ signal region. The highest-p_{T} bin includes the overflow.

10.2 Cross Section Definition

The number of candidates in the signal region (N) is related to the $W^{\pm}Z$ production cross section ($\sigma_{W^{\pm}Z}$) by:

$$N = \mathcal{L} \times \sigma_{W^{\pm}Z} \times \mathcal{B}r\left(W^{\pm}Z \to \ell^{\pm}\nu_{\ell}\ell'^{+}\ell'^{-}\right) \times A_{W^{\pm}Z} \times C_{W^{\pm}Z} \times (1 + f_{\tau}) + N_{\mathrm{bkg}}, \quad (10.1)$$

which can be solved for $\sigma_{W^{\pm}Z}$ as:

$$\sigma_{W^{\pm}Z} = \frac{N - N_{\mathrm{bkg}}}{\mathcal{L} \times \mathcal{B}r\left(W^{\pm}Z \to \ell^{\pm}\nu_{\ell}\ell'^{+}\ell'^{-}\right) \times A_{W^{\pm}Z} \times C_{W^{\pm}Z} \times (1 + f_{\tau})}. \quad (10.2)$$

Here $\mathcal{L}$ is the integrated luminosity, $\mathcal{B}r\left(W^{\pm}Z \to \ell^{\pm}\nu_{\ell}\ell'^{+}\ell'^{-}\right)$ is the branching fraction for $W^{\pm}Z$ decaying to electrons and muons only, $A_{W^{\pm}Z}$ is the fiducial acceptance, $C_{W^{\pm}Z}$ is the detection efficiency, f_{τ} is the fractional enhancement in the signal region due to the contribution of tauonic decay modes, and N_{bkg} is the background expectation. The luminosity is calculated per Section 2.2.4, the branching fraction is taken to be the product

of the $W^{\pm} \to \ell^{\pm}\nu_{\ell}$ and $Z \to \ell^{+}\ell^{-}$ branching fractions [38], $A_{W^{\pm}Z}$ is calculated using a combination of MCFM and the simulation, $C_{W^{\pm}Z}$ and f_{τ} are estimated using simulation, and the background is calculated per Chapter 8. Since the Z/γ^{*} lineshape is divergent at low mass, $\sigma_{W^{\pm}Z}$ is defined to be the total production cross section for Z-bosons with mass between 66 and 116 GeV.

10.2.1 Fiducial Acceptance Calculation

The fiducial acceptance ($A_{W^{\pm}Z}$) is defined as the probability for a produced $W^{\pm}Z$ pairs to fall within the phase-space region, called the fiducial volume, corresponding to the instrumented region of the ATLAS detector. The fiducial volume for this analysis is defined as:

- $|m^{Z} - m^{Z}_{\mathrm{PDG}}| < 10$ GeV
- $m^{W}_{\mathrm{T}} > 20$ GeV
- $p^{\nu}_{\mathrm{T}} > 25$ GeV
- Charged leptons from Z with $p_{\mathrm{T}} > 15$ GeV
- Charged lepton from W with $p_{\mathrm{T}} > 20$ GeV
- All charged leptons with $|\eta| < 2.5$
- $\Delta R(\ell, \ell') > 0.3$ for all pairs of charged leptons

$A_{W^{\pm}Z}$ is calculated as the product of the parton-level acceptance and a PS correction factor. The parton-level acceptance is calculated as the ratio of the cross section calculated using MCFM and CT10 in the two phase space volumes (viz. fiducial and total). The PS correction is calculated as the ratio of the number of $W^{\pm}Z$ events in the fiducial volume after the PS to the number before the PS, using the MC@NLO+Jimmy+Herwig simulated sample generated with SM couplings. All leptons are dressed by adding back the 4-momenta of any QED FSR within a cone of $\Delta R = 0.1$ before events are evaluated as being in the fiducial volume after the PS. The parton-level and PS-corrected fiducial acceptance for each channel is given in Table 10.2. At the parton level, all four flavor channels have the same acceptance, but after the PS, a difference is found between the different flavor channels.

10.2.2 Detection Efficiency Calculation

The detection efficiency ($C_{W^{\pm}Z}$) is defined as the probability of detecting a $W^{\pm}Z$ candidate given that one was produced in the fiducial volume. It can be calculated as:

$$C_{W^{\pm}Z} = \frac{N^{\mathrm{MC}}\,(\text{Signal Region}) \times \mathrm{SF}}{N^{\mathrm{MC}}\,(\text{Fiducial Volume})}, \tag{10.3}$$

Channel	$e^{\pm}\nu_e e^+e^-$	$e^{\pm}\nu_e \mu^+\mu^-$	$\mu^{\pm}\nu_\mu e^+e^-$	$\mu^{\pm}\nu_\mu \mu^+\mu^-$
A_{WZ}(parton-level)	0.352	0.352	0.352	0.352
A_{WZ}(after PS)	0.330	0.332	0.333	0.338
C_{WZ}	0.380	0.525	0.548	0.780
$A_{WZ} \times C_{WZ}$	0.125	0.174	0.182	0.263

Table 10.2: Fiducial acceptance and detection efficiency for each flavor channel.

where SF is the net effect of all SF applied per Section 9.1.5. The value of $C_{W^{\pm}Z}$ for each of the flavor channels, along with the product $A_{W^{\pm}Z} \times C_{W^{\pm}Z}$ is given in Table 10.2.

10.2.3 Tauonic Decay Modes

The contribution of tauonic decay modes to the signal expectation is calculated using simulation. The expected signal contribution from τX (prompt e/μ) decay modes is given on the final (penultimate) line of Table 7.1.

10.3 Cross Section Extraction

Taking N to be the observed number of candidates, a Poisson likelihood function can be constructed from Equation 10.2 to extract the $W^{\pm}Z$ production cross section. Allowing for fluctuations in the various parameters based on their uncertainties using Gaussian nuisance parameters, a likelihood maximization fit is performed, the solution of which is the measured $W^{\pm}Z$ production cross section.

10.3.1 Likelihood Function

The Poisson probability to observe a certain number of candidate events in the i^{th} channel (N^i_{obs}), given an expected event yield (N^i_{exp}), can be written as:

$$P\left(N^i_{\text{obs}}; N^i_{\text{exp}}\right) = \frac{\left(N^i_{\text{exp}}\right)^{N^i_{\text{obs}}} \cdot e^{-N^i_{\text{exp}}}}{N^i_{\text{obs}}!}. \tag{10.4}$$

Retrospectively, once N^i_{obs} has been observed in each channel, the interesting quantity becomes the likelihood (L) that N^i_{exp}, treated as a function of the cross section per Equation 10.1, would produce N^i_{obs}. This can be written as the product of the Poisson probability for each channel:

$$L\left(\sigma_{W^{\pm}Z}\right) = \prod_{i=1}^{4} \frac{\left(N^i_{\text{exp}}\left(\sigma_{W^{\pm}Z}\right)\right)^{N^i_{\text{obs}}} \cdot e^{-N^i_{\text{exp}}\left(\sigma_{W^{\pm}Z}\right)}}{N^i_{\text{obs}}!} \tag{10.5}$$

The measured cross section is then the value of $\sigma_{W^{\pm}Z}$ that maximizes the likelihood function (i.e. the value at which the probability of producing the observed result is highest).

10.3.2 Nuisance Parameters

If N^i_{exp} was known exactly, Equation 10.5 would suffice. However, the value of N^i_{exp} has several uncertainties, as described in Chapter 9, that need to be taken into account. A straightforward method of accomplishing this is to posit a set of parameters ($\{x_k\}$), called nuisance parameters, each of which is assumed to be normally distributed. Each x_k is taken to represent one of either the simulation uncertainties listed in Table 9.1, the statistical uncertainty in the signal or background MC samples, or the total uncertainty in one of the two data-driven background estimation methods (per Section 9.2). If the fractional uncertainties in the number of expected signal events in the i^{th} channel are denoted $\left\{S^i_k\right\}$ and the fractional uncertainties in the background expectation are denoted $\left\{B^i_k\right\}$, the expected numbers of signal (N^i_{sig}) and background (N^i_{bkg}) events can be written:

$$N^i_{\text{sig}}\left(\{x_k\}\right) = N^i_{\text{sig}}\left(0\right) \times \left[1 + \sum_{k=1}^{n}\left(x_k \cdot S^i_k\right)\right], \tag{10.6}$$

$$N^i_{\text{bkg}}\left(\{x_k\}\right) = N^i_{\text{bkg}}\left(0\right) \times \left[1 + \sum_{k=1}^{n}\left(x_k \cdot B^i_k\right)\right]. \tag{10.7}$$

S^i_k (B^i_k) is zero if the k^{th} uncertainty does not affect the signal (background) expectation in the i^{th} channel. Both S^i_k and B^i_k are estimated per Chapter 9 and rounded to the nearest 0.1%. The resulting likelihood function, with the inclusion of the aforementioned Gaussian constraints on $\{x_k\}$, can be written:

$$L\left(\sigma_{W^{\pm}Z}, \{x_k\}\right) = \prod_{i=1}^{4}\left(\frac{\left(N^i_{\text{exp}}\left(\sigma_{W^{\pm}Z}, \{x_k\}\right)\right)^{N^i_{\text{obs}}} \cdot e^{-N^i_{\text{exp}}\left(\sigma_{W^{\pm}Z}, \{x_k\}\right)}}{N^i_{\text{obs}}!}\right) \times \prod_{k=1}^{n}\left(e^{-\frac{x_k^2}{2}}\right). \tag{10.8}$$

10.3.3 Minimization

The MINUIT program [42], is used to measure both the fiducial cross section ($\sigma^{\text{fid}}_{W^{\pm}Z} \equiv \sigma_{W^{\pm}Z} \times \mathcal{B}r\left(W^{\pm}Z \to \ell^{\pm}\nu_{\ell}\ell'^{+}\ell'^{-}\right) \times A_{W^{\pm}Z}$), which excludes the uncertainty in $A_{W^{\pm}Z}$, and the total cross section ($\sigma_{W^{\pm}Z}$) assuming the values of $A_{W^{\pm}Z}$ listed in Table 10.2. Except in the case of luminosity, the upwards or downwards uncertainty in either cross section due to the k^{th} source is calculated by shifting x_k until it produces a shift in the negative log of the likelihood of 0.5, finding a new value of the cross section by minimizing $-\log L$ while holding the nuisance parameters constant at the shifted values, and evaluating the change in the cross section; the uncertainty in the cross sections due to

the uncertainty in the luminosity is taken to be the fractional uncertainty in the luminosity. The uncertainties in the measured cross section are given in Table 10.3. The measured fiducial and total cross sections are:

$$\sigma^{\text{fid}}_{W^{\pm}Z} = 92.31^{+6.66}_{-6.33}(\text{stat.})^{+4.31}_{-4.26}(\text{syst.}) \pm 1.85(\text{lumi.})\ \text{fb}, \tag{10.9}$$

$$\sigma_{W^{\pm}Z} = 19.00^{+1.38}_{-1.30}(\text{stat.})^{+0.92}_{-0.90}(\text{syst.}) \pm 0.38(\text{lumi.})\ \text{pb}, \tag{10.10}$$

which agree with the SM expectations, calculated per Section 10.2.1, of 85^{+7}_{-9} fb and $17.6^{+1.1}_{-1.0}$ pb, respectively.

Source	$\sigma^{\text{fid}}_{W^\pm Z}$	$\sigma_{W^\pm Z}$
μ reconstruction efficiency	$^{+0.52}_{-0.53}$	$^{+0.53}_{-0.53}$
μ p_{T} scale & resolution	$^{+0.07}_{-0.07}$	$^{+0.07}_{-0.07}$
μ isolation & impact param.	$^{+0.39}_{-0.40}$	$^{+0.40}_{-0.40}$
e reconstruction efficiency	$^{+1.12}_{-1.11}$	$^{+1.10}_{-1.09}$
e identification efficiency	$^{+1.61}_{-1.57}$	$^{+1.57}_{-1.55}$
e isolation & impact param.	$^{+0.62}_{-0.63}$	$^{+0.61}_{-0.60}$
e energy scale	$^{+0.25}_{-0.25}$	$^{+0.24}_{-0.24}$
e energy resolution	$^{+0.04}_{-0.04}$	$^{+0.04}_{-0.04}$
$E_{\text{T}}^{\text{miss}}$ topocluster energy scale	$^{+0.36}_{-0.37}$	$^{+0.36}_{-0.36}$
$E_{\text{T}}^{\text{miss}}$ jet energy scale	$^{+0.11}_{-0.11}$	$^{+0.11}_{-0.11}$
$E_{\text{T}}^{\text{miss}}$ jet energy resolution	$^{+0.32}_{-0.32}$	$^{+0.32}_{-0.32}$
$E_{\text{T}}^{\text{miss}}$ pile-up	$^{+0.20}_{-0.20}$	$^{+0.20}_{-0.20}$
Trigger	$^{+0.20}_{-0.20}$	$^{+0.20}_{-0.20}$
Signal MC statistics	$^{+0.50}_{-0.51}$	$^{+0.50}_{-0.50}$
Background MC statistics	$^{+0.43}_{-0.42}$	$^{+0.43}_{-0.42}$
Background fake-factor method	$^{+3.05}_{-3.04}$	$^{+3.06}_{-3.02}$
Background scale-factor method	$^{+1.26}_{-1.26}$	$^{+1.26}_{-1.25}$
Event generator	-	$^{+0.40}_{-0.40}$
PDF	-	$^{+1.21}_{-1.18}$
QCD scale	-	$^{+0.40}_{-0.40}$
Total excl. luminosity	$^{+4.67}_{-4.62}$	$^{+4.85}_{-4.76}$
Luminosity	1.8	1.8

Table 10.3: Systematic uncertainties (%) on the fiducial and total cross sections from various sources.

Chapter 11
Limits on Anomalous Trilinear Gauge Couplings

The aTGC described in Section 1.2.2 are zero in the SM. Limits on the deviation from zero are set for each of the coupling. In improvement over the previous iteration of this analysis [43], in which limits were set by comparing the integrated event yields to the SM expectation, the limits in this analysis are set using the differential distribution of Z-boson p_{T}. First, the p_{T} distribution is calculated as a function of the coupling. Then, a likelihood profile is generated for each coupling. Finally, the 95% confidence interval is extracted for each of the couplings.

11.1 Z-Boson p_{T} Distribution

The expected Z-boson p_{T} distributions for SM couplings as well as three sample anomalous couplings are shown in Figure 11.1. Since the $W^{\pm}Z$-system is produced from partons with relatively low-p_{T}, the Z-boson p_{T} scales roughly with the total momentum transfer in the hard scattering process. Since the hypothetical anomalous particles, that would mediate the interactions for which aTGCs are an effective model, would tend to be relatively high-mass, the total momentum transfer in such interactions is commensurately large, so the Z-boson p_{T} distribution is enhanced at higher momentum values, as can be seen in the overflow bin of the figure. Thus, the shape of the distribution is sensitive to the presence of aTGCs. The p_{T} distribution is calculated in 30 GeV bins up to 180 GeV, with the overflow bin truncated at 2 TeV.

As described in Section 6.4, the weight of each event in the MC samples generated with non-SM couplings is calculated as a linear function of the weights from the 10 terms (1 SM plus 9 anomalous) that contribute to the cross section, with coefficients dependent on the couplings, per Equation 6.1. Thus, the expected distribution can be readily calculated as a function of the couplings by determining the contribution to the distribution from each of the 10 weights separately and then combining them into the expected Z-boson p_{T}

distribution. The expected signal yield in the i^{th} bin (N^i) is then:

$$\begin{aligned} N^i \;=\; N_0^i \;&+ \left(\Delta g_1^Z\right)^2 N_1^i + \left(\Delta\kappa^Z\right)^2 N_2^i + \left(\lambda^Z\right)^2 N_3^i \\ &+ 2\Delta g_1^Z N_4^i + 2\Delta\kappa^Z N_5^i + 2\lambda^Z N_6^i \\ &+ 2\Delta g_1^Z \Delta\kappa^Z N_7^i + 2\Delta g_1^Z \lambda^Z N_8^i + 2\Delta\kappa^Z \lambda^Z N_9^i, \end{aligned} \tag{11.1}$$

where N_j^i is the sum, over simulated events in the signal region that have Z-boson p_{T} in the range of the i^{th} bin, of $w_j \times (-1)^s \times w_{\text{prw}} \times \text{SF}$, where $(-1)^s$ is the MC@NLO event phase, the w_{prw} weight used to accomplish the pile-up reweighting described in Section 9.1.4, and SF is the product of all relevant SFs in the event.

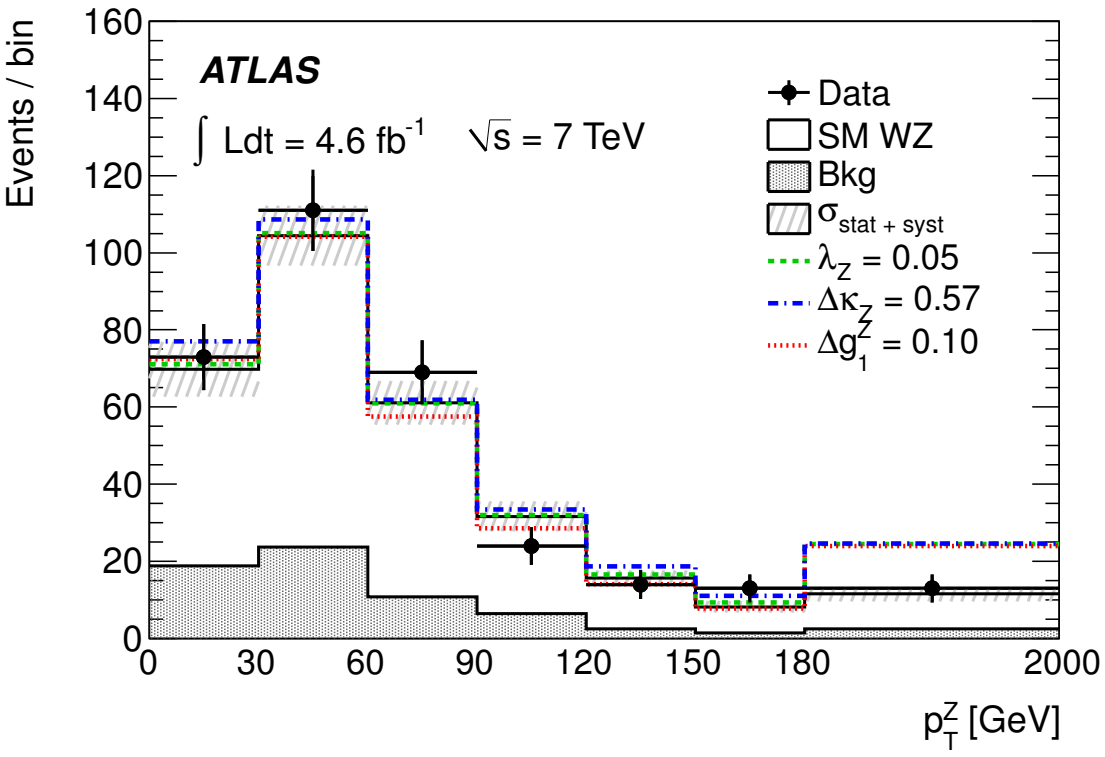

Figure 11.1: p_{T} distribution of Z-bosons in $W^{\pm}Z$ candidate events. The solid-line histogram shows the SM expectation, including both signal (open) and background (hashed). The dashed-line histograms show the expectations for sample values of the three aTGCs.

The simulated sample is generated using a form-factor:

$$\alpha \equiv \frac{\alpha_\infty}{\left(1 + \frac{\hat{s}}{\Lambda^2}\right)^2}, \tag{11.2}$$

where α_∞ is the bare coupling, $\hat{s}$ is the square of the invariant mass of the $W^\pm Z$-system generated in the ME calculation, and Λ is an arbitrary cut-off scale, set by default to 100 TeV in the event generation. The TGC limits in this analysis are calculated using p_T distributions as determined both with the couplings in Equation 11.1 being the bare couplings (i.e. using an infinite cut-off) and with the couplings calculated using a 2 TeV cut-off scale. The weights (w_j) for a given cut-off scale are determined by multiplying each of the generated weights by the ratio of the form-factors at the generated and used cut-off scales for each factor of a coupling by which the weight is multiplied in Equation 6.1.

11.2 aTGC Limits

Frequentist limits on aTGCs are set using the profile likelihood method, in which a likelihood function is constructed as a function of the couplings, a test statistic called the likelihood ratio is defined, the likelihood profile versus coupling is constructed using that test statistic, and limits are extracted.

11.2.1 Likelihood Function

The likelihood of observing a given p_T distribution, which is the product over bins of the Poisson probability of observing N^i_obs given N^i_exp, where i now denotes particular p_T range (i.e. bin), times the product of the Gaussian constraints on each of the nuisance parameters $\{x_k\}$, is:

$$L\left(\alpha, \{x_k\}\right) = \prod_{i=1}^{7} \left(\frac{\left(N^i_\mathrm{exp}\left(\alpha, \{x_k\}\right)\right)^{N^i_\mathrm{obs}} \cdot e^{-N^i_\mathrm{exp}(\alpha, \{x_k\})}}{N^i_\mathrm{obs}!} \right) \times \prod_{k=1}^{n} \left(e^{-\frac{x_k^2}{2}} \right). \tag{11.3}$$

where α is the coupling. In this analysis, a limit is set on each coupling setting the other two couplings to the SM values. When extracting the limits, L is maximized by minimizing $-\log L$.

11.2.2 Likelihood Ratio

The likelihood function is used to define a test statistic called the likelihood ratio ($q\left(\alpha\right)$), defined for a given Z-boson p_T distribution as the ratio of the maximum likelihood at a fixed value of the coupling to the maximum likelihood determined while allowing the coupling to float during MINUIT minimization:

$$q\left(\alpha\right) \equiv \frac{L\left(\alpha, \mathbf{x}'\right)}{L\left(\alpha_0, \mathbf{x}_0\right)}, \tag{11.4}$$

where α_0 is the coupling value that maximizes the likelihood (with the set of nuisance parameters $\mathbf{x}_0$) and $\mathbf{x}'$ is the set of nuisance parameters that maximizes the likelihood when

Coupling	$\Lambda = 2$ TeV	no form factor
Δg_1^Z	$[-0.074, 0.133]$	$[-0.057, 0.093]$
$\Delta\kappa^Z$	$[-0.42, 0.69]$	$[-0.37, 0.57]$
λ^Z	$[-0.064, 0.066]$	$[-0.046, 0.047]$

Table 11.1: Observed limits on the three aTGCs at both 2 TeV and infinite cut-off scales.

the coupling is fixed at α.

11.2.3 Likelihood Profile

A likelihood profile $p(\alpha)$ is generated by calculating its value at each value of the couplings. First, $q_{\text{obs}}(\alpha)$ is defined as $q(\alpha)$ for the observed p_{T} distribution. Then, 10000 pseudo-experiments are generated at that value of α as follows: the nuisance parameters are Gaussian fluctuated around $\mathbf{x}'$, and an "observed" yield for each pseudo-experiment is generated using the Poisson distribution for the expected yield predicted by the coupling α and the fluctuated set of nuisance parameters. Finally, at each value of the coupling α, the value of the likelihood profile $p(\alpha)$ is calculated as the fraction of the pseudo-experiments that had a smaller likelihood ratio than $q_{\text{obs}}(\alpha)$.

11.2.4 Limit Extraction

Since the couplings can, in principle, assume negative values, the limits are extracted at the 95% confidence level (C.L.) as a two-sided confidence interval (C.I.). The C.I. is defined as the region, or set of regions (since N^i_{exp} is a quadratic function of α, per Equation 11.1), within which $p(\alpha)$ is $\geq 5\%$. The C.I. is thus constructed by scanning through values of α. The measured limits for all three aTGCs, at both the 2 TeV (i.e. supposing that a hypothetical 2 TeV particle is the source of the anomalous interactions) and infinite (i.e. supposing that the hypothetical particle producing the anomalous interactions is far above the energy scale of the LHC) cut-off scales, are shown in Table 11.1, and a comparison of the limits measured in this analysis to those measured at the Tevatron is shown in Figure 11.2. In all cases, the result is consistent with the SM couplings.

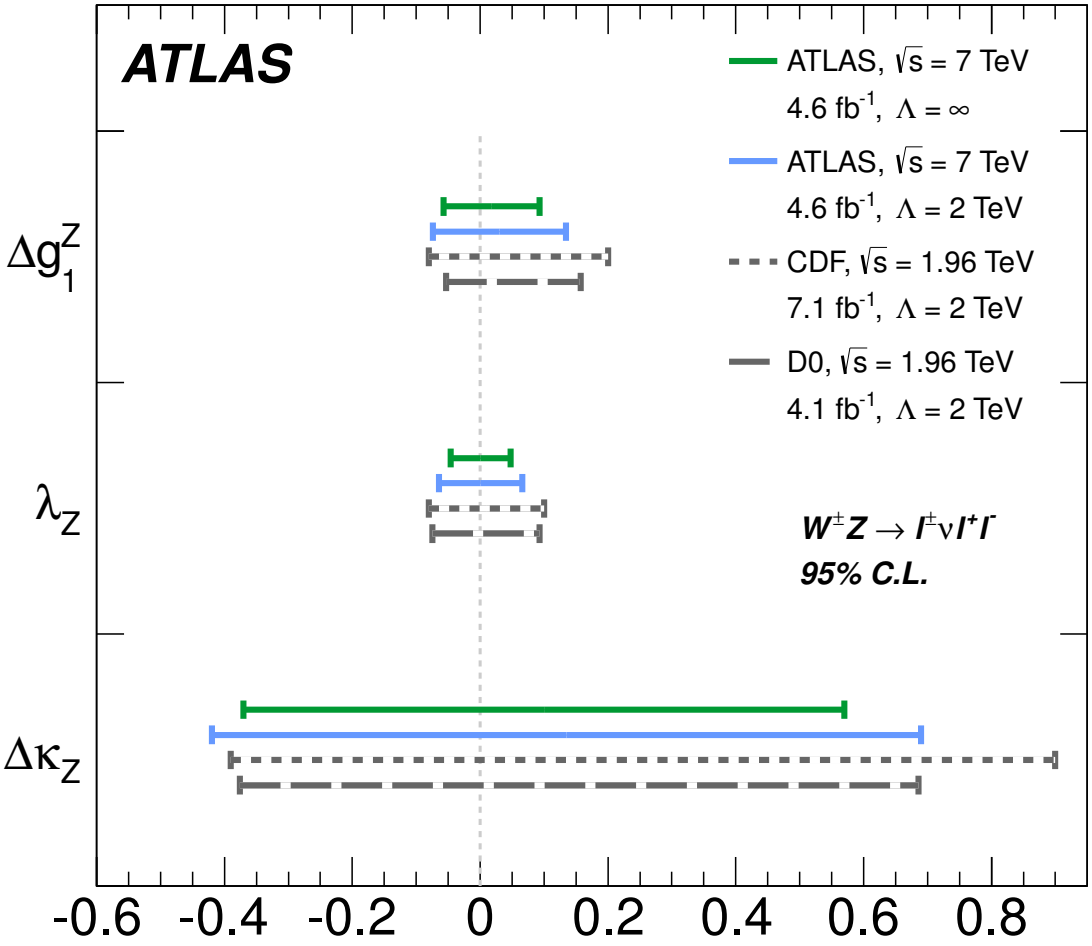

Figure 11.2: A comparison of the limits on the three aTGCs measured in this analysis to those measured at the Tevatron.

Chapter 12
Conclusion

$W^{\pm}Z$ production in proton-proton collisions at $\sqrt{s} = 7$ TeV has been studied, in leptonic final states, using 4.64 fb^{-1} of ATLAS data. The production cross section has been determined to be $19.0^{+1.4}_{-1.3}$(stat.)$\pm$0.9(syst.)$\pm$0.4(lumi.), in agreement with the SM expectation of $17.6^{+1.1}_{-1.0}$ pb. A search for aTGC has been conducted and limits have been set at the 95% C.L.; the result is consistent with the SM couplings.

Bibliography

[1] M. E. Peskin and D. V. Schroeder, *An introduction to quantum field theory*. Westview Press, 1995.

[2] J. D. Griffiths, *Introduction to elementary particle physics*. Wiley VCH, 2008.

[3] CDF Collaboration, T. Aaltonen et al., *Measurement of the WZ cross section and triple gauge couplings in $p\bar{p}$ collisions at $\sqrt{s} = 1.96$ TeV*, Phys. Rev. **D 86** (2012) 031104, arXiv:1202.6629 [hep-ex].

[4] DØ Collaboration, V. M. Abazov et al., *Measurement of the $WZ \to \ell\nu\ell\ell$ cross section and limits on anomalous triple gauge couplings in $p\bar{p}$ collisions at $\sqrt{s} = 1.96$ TeV*, Phys. Lett. **B 695** (2011) 67, arXiv:1006.0761 [hep-ex].

[5] K. Hagiwara, R. D. Peccei, D. Zeppenfeld, and K. Hikasa, *Probing the weak boson sector in $e^+e^- \to W^+W^-$*, Nucl. Phys. **B 282** (1987) 253.

[6] J. Ellison and J. Wudka, *Study of trilinear gauge boson couplings at the Tevatron collider*, Ann. Rev. Nucl. Part. Sci. **48** (1998) 33, arXiv:hep-ph/9804322 [hep-ph].

[7] ATLAS Collaboration, *The ATLAS experiment at the CERN large hadron collider*, JINST **3** (2008) S08003.

[8] L. Evans, P. Bryant, et al., *LHC machine*, JINST **3** (2008) S08001.

[9] V. Cindro et al., *The ATLAS beam conditions monitor*, JINST **3** (2008) P02004.

[10] ATLAS Collaboration, *Luminosity determination with the ATLAS detector*, Eur. Phys. J. **C 71** (2011) 1630, arXiv:1101.2185 [hep-ex].

[11] ATLAS Collaboration, *Performance of the ATLAS inner detector track and vertex reconstruction in the high pile-up LHC environment*, Tech. Rep. ATLAS-CONF-2012-042, CERN, Geneva, 2012.

[12] W. Lampl et al., *Calorimeter clustering algorithms: description and performance*, Tech. Rep. ATL-LARG-PUB-2008-002, CERN, Geneva, 2008.

[13] ATLAS Collaboration, *Muon performance in minimum bias pp collision data at* $\sqrt{s}$ = *7 TeV with ATLAS*, Tech. Rep. ATLAS-CONF-2010-036, CERN, Geneva, 2010.

[14] ATLAS Collaboration, *Electron performance measurements with the ATLAS detector using the 2010 LHC proton-proton collision data*, Eur. Phys. J. **C 72** (2012) 1909, arXiv:1110.3174 [hep-ex].

[15] M. Cacciari, G. P. Salam, and G. Soyez, *The anti-*k_t *jet clustering algorithm*, JHEP **0804** (2008) 063, arXiv:0802.1189 [hep-ph].

[16] ATLAS Collaboration, *Performance of missing transverse momentum reconstruction in proton-proton collisions at 7 TeV with ATLAS*, Eur. Phys. J. **C 72** (2012) 1844, arXiv:1108.5602 [hep-ex].

[17] ATLAS Collaboration, *The ATLAS simulation infrastructure*, Eur. Phys. J. **C 70** (2010) 823, arXiv:1005.4568 [physics.ins-det].

[18] H.-L. Lai et al., *New parton distributions for collider physics*, Phys. Rev. **D 82** (2010) 074024, arXiv:1007.2241 [hep-ph].

[19] S. Frixione and B. R. Webber, *Matching NLO QCD computations and parton shower simulations*, JHEP **0206** (2002) 029, arXiv:hep-ph/0204244 [hep-ph].

[20] S. Frixione, F. Stoeckli, P. Torrielli, B. R. Webber, and C. D. White, *The MC@NLO 4.0 event generator*, arXiv:1010.0819 [hep-ph].

[21] J. Butterworth, J. R. Forshaw, and M. Seymour, *Multiparton interactions in photoproduction at HERA*, Z. Phys. **C 72** (1996) 637, arXiv:hep-ph/9601371 [hep-ph].

[22] G. Corcella et al., *HERWIG 6: an event generator for hadron emission reactions with interfering gluons (including supersymmetric processes)*, JHEP **0101** (2001) 010, arXiv:hep-ph/0011363 [hep-ph].

[23] S. Jadach, Z. Was, R. Decker, and J. H. Kuhn, *The tau decay library TAUOLA: version 2.4*, Comput. Phys. Commun. **76** (1993) 361.

[24] P. Golonka and Z. Was, *PHOTOS Monte Carlo: a precision tool for QED corrections in Z and W decays*, Eur. Phys. J. **C 45** (2006) 97, arXiv:hep-ph/0506026 [hep-ph].

[25] S. Agostinelli et al., *GEANT4: a simulation toolkit*, Nucl. Instrum. Meth. **A 506** (2003) 250.

[26] T. Sjostrand et al., *High-energy physics event generation with PYTHIA 6.1*, Comput. Phys. Commun. **135** (2001) 238, arXiv:hep-ph/0010017 [hep-ph].

[27] J. Pumplin et al., *New generation of parton distributions with uncertainties from global QCD analysis*, JHEP **0207** (2002) 012, arXiv:hep-ph/0201195 [hep-ph].

[28] J. M. Campbell and R. K. Ellis, *An update on vector boson pair production at hadron colliders*, Phys. Rev. **D 60** (1999) 113006, arXiv:hep-ph/9905386 [hep-ph].

[29] M. L. Mangano, M. Moretti, F. Piccinini, R. Pittau, and A. D. Polosa, *ALPGEN, a generator for hard multiparton processes in hadronic collisions*, JHEP **0307** (2003) 001, arXiv:hep-ph/0206293 [hep-ph].

[30] J. Alwall et al., *MadGraph/MadEvent v4: the new web generation*, JHEP **0709** (2007) 028, arXiv:0706.2334 [hep-ph].

[31] T. Gleisberg et al., *Event generation with SHERPA 1.1*, JHEP **0902** (2009) 007, arXiv:0811.4622 [hep-ph].

[32] A. D. Martin, W. J. Stirling, and R. S. Thorne, *MRST partons generated in a fixed-flavour scheme*, Phys. Lett. **B 636** (2006) 259, arXiv:hep-ph/0603143 [hep-ph].

[33] M. Aliev et al., *HATHOR: HAdronic Top and Heavy quarks crOss section calculatoR*, Comput. Phys. Commun. **182** (2011) 1034, arXiv:1007.1327 [hep-ph].

[34] J. M. Campbell and R. K. Ellis, $t\bar{t}W^{\pm}$ *production and decay at NLO*, JHEP **1207** (2012) 052, arXiv:1204.5678 [hep-ph].

[35] A. Lazopoulos, T. McElmurry, K. Melnikov, and F. Petriello, *Next-to-leading order QCD corrections to* $t\bar{t}Z$ *production at the LHC*, Phys. Lett. **B 666** (2008) 62, arXiv:0804.2220 [hep-ph].

[36] R. Hamberg, W. van Neerven, and T. Matsuura, *A complete calculation of the order* α_S^2 *correction to the Drell-Yan K factor*, Nucl. Phys. **B 359** (1991) 343. Erratum-ibid. **B 644** (2002) 403.

[37] C. Anastasiou, L. J. Dixon, K. Melnikov, and F. Petriello, *High precision QCD at hadron colliders: electroweak gauge boson rapidity distributions at NNLO*, Phys. Rev. **D 69** (2004) 094008, arXiv:hep-ph/0312266 [hep-ph].

[38] Particle Data Group Collaboration, K. Nakamura et al., *Review of particle physics*, J. Phys. **G 37** (2010) 075021.

[39] T. Melia, P. Nason, R. Rontsch, and G. Zanderighi, W^+W^-, WZ *and* ZZ *production in the POWHEG BOX*, JHEP **1111** (2011) 078, arXiv:1107.5051 [hep-ph].

[40] A. Martin, W. Stirling, R. Thorne, and G. Watt, *Parton distributions for the LHC*, Eur. Phys. J. **C 63** (2009) 189, arXiv:0901.0002 [hep-ph].

[41] ATLAS Collaboration, *Measurement of* WZ *production in proton-proton collisions at* $\sqrt{s} = 7$ *TeV with the ATLAS detector*, Eur. Phys. J. **C 72** (2012) 2173, arXiv:1208.1390 [hep-ex].

[42] F. James, *MINUIT - function minimization and error analysis.* CERN Program Library entry D506, Geneva, 1998.

[43] ATLAS Collaboration, *Measurement of the* $W^{\pm}Z$ *production cross section and limits on anomalous triple gauge couplings in proton-proton collisions at* $\sqrt{s} = 7$ *TeV with the ATLAS detector*, Phys. Lett. **B 709** (2012) 341, arXiv:1111.5570 [hep-ex].